Heliyon 9 (2023) e17735

Contents lists available at ScienceDirect

Heliyon

journal homepage: www.cell.com/heliyon

# Optical coherence tomography image despeckling based on tensor singular value decomposition and fractional edge detection

Ying Fang [a], Xia Shao [a], Bangquan Liu [c], Hongli Lv [a,b,*]

[a] School of Information Technology, Shangqiu Normal University, Shangqiu, 476000, China
[b] College of Big Data and Software Engineering, Zhejiang Wanli University, Ningbo, 315100, China
[c] College of Digital Technology and Engineering, Ningbo University of Finance and Economics, Ningbo, 315100, China

ARTICLE INFO

*Keywords:*
Fractional edge detection
*t*-SVD
Optical coherence tomography
Speckle noise

ABSTRACT

Optical coherence tomography (OCT) imaging is a technique that is frequently used to diagnose medical conditions. However, coherent noise, sometimes referred to as speckle noise, can dramatically reduce the quality of OCT images, which has an adverse effect on how OCT images are used. In order to enhance the quality of OCT images, a speckle noise reduction technique is developed, and this method is modelled as a low-rank tensor approximation issue. The grouped 3D tensors are first transformed into the transform domain using tensor singular value decomposition (*t*-SVD). Then, to cut down on speckle noise, transform coefficients are thresholded. Finally, the inverse transform can be used to produce images with speckle suppression. To further enhance the despeckling results, a feature-guided thresholding approach based on fractional edge detection and an adaptive backward projection technique are also presented. Experimental results indicate that the presented algorithm outperforms several comparison methods in relation to speckle suppression, objective metrics, and edge preservation.

## 1. Introduction

As an important non-ionizing optical imaging modality, optical coherence tomography imaging has many advantages, such as high safety, fast scanning speed, and high resolution [1,2]. OCT is now a significant medical diagnostic tool, particularly for the diagnosis and treatment of eye diseases [3,4]. However, because of the limits and defects of low-coherence interferometry and imaging equipment, the obtained OCT images are susceptible to coherent noise, usually called multiplicative speckle noise, which gives rise to significant limitations on their illness diagnosis [5,6]. Furthermore, the degraded quality of the OCT images might have a significant impact on the processing that follows, such as the segmentation and measurement of lesions. Therefore, speckle reduction for OCT images is essential to effectively help physicians accurately diagnose relevant diseases [7,8]. However, keeping fine image features and effectively removing speckle noise remains a difficult task in the area of the processing of OCT images.

To effectively reconstruct OCT images from noisy versions, researchers have proposed many different methods, which are generally grouped into two categories: hardware-based approaches [9–15] and software-based approaches [16–43]. However, the former category of approaches [9–15] requires significant modifications to existing imaging system hardware, which makes them less applicable to ordinary commercialized imaging equipment based on OCT technologies. By contrast, software-based post-processing approaches [16–43] are more efficient and low-cost. For this reason, the proposed method mainly focuses on the technique related to

* Corresponding author. School of Information Technology, Shangqiu Normal University, Shangqiu, 476000, China
*E-mail address:* honglilv@foxmail.com (H. Lv).

https://doi.org/10.1016/j.heliyon.2023.e17735
Received 24 December 2022; Received in revised form 26 June 2023; Accepted 27 June 2023
Available online 29 June 2023

the latter.

In the literature on software-based methods, researchers are mainly concerned with designing a certain algorithm in a certain space or transformation domain, for instance, spatial filtering methods [16,17], partial differential equation (PDE) methods [18–21], wavelet decomposition methods [22–25], probabilistic methods [26–28], etc. Each of these methods has its advantages and disadvantages. For example, spatial filtering methods generally work fast but tend to blur image details. PDE methods can maintain the detailed features of OCT images better while suppressing noise, but they often produce staircase effects and block artifacts. The wavelet decomposition method is a classical speckle noise suppression technique and has better performance on speckle reduction. However, the fixed wavelet basis cannot represent the rich image details. Therefore, unnecessary visual artifacts are always introduced in the denoised image. Probabilistic methods can take full advantage of the probability distribution of OCT images, but an accurate estimate of this distribution cannot be easily obtained in the presence of severe speckle noise pollution. These techniques are not effective in both preserving OCT image features and suppressing speckle noise. One reason could be the inadequacy of prior information or the limited representation of fixed bases. In recent years, exploring nonlocal self-similarity, sparsity, and low-rank priors has exhibited impressive performance in speckle reduction of OCT images. Some examples of such methods are nonlocal mean methods [29–31], sparse representation methods [32–36], and low-rank approximation methods [37–39]. Compared to traditional methods, these methods can obtain better despeckling results. However, some disadvantages still exist for these methods in despeckling OCT images. Nonlocal mean methods blur the fine structures of OCT images. As for sparse representation methods, the dependence on the learned dictionary limits their usability. If there is a previously unobserved feature in the given images, the dictionary cannot adequately represent and rebuild it. In addition, the inappropriateness of threshold selection can lead to over-smoothed or under-smoothed results of low-rank approximation methods. On the other hand, deep learning techniques are advancing at a rapid pace and have achieved good despeckling results [40–43]. However, the acquisition of a rich variety and a huge amount of training data can be very time-consuming and resource-intensive.

As a novel theoretical and computational framework of tensor decomposition, *t*-SVD [44,45] can effectively extract the orientation information of multidimensional data and has excellent performance in the processing of digital images [46–51]. In this work, a two-stage despeckling method is proposed by using *t*-SVD and fractional edge detection that aims to effectively reduce the impact of speckle noise. Other than that, we also try to restore the detail structures of images. Specifically, in the first stage, the nonlocal method is first used to find image patches that are similar to each other, and these similar patches are grouped into 3D blocks, which are then converted into the transform domain by the *t*-SVD method. Next, transform coefficients, namely singular values accounting for the main signals, are thresholded to reduce speckle noise. Finally, the inverse transform and aggregation can be used to create speckle suppression images. The iterative regularization technique based on the backward projection method [38,52] is a widely used strategy to increase the despeckling performance in low-rank approximation methods. However, one of the drawbacks of such methods is that the projection parameter is often established as a fixed constant without taking into account the inherent feature properties, e.g., edge information. To address this issue, the despeckling results of the first stage are refined by an adaptive backward projection method. That is, the noisy OCT image, inputted in the second stage, is re-modified based on the detected edge information, which can be obtained by the proposed fractional-order diffusion equation. In addition, an adaptive thresholding strategy is also proposed by using the edge features. The motivation is as follows: in the vicinity of edges, threshold needs to be assigned a smaller value to better retain image structural features. In the flat regions, the threshold needs to be assigned a higher value to provide better smoothing results.

The remainder of this paper is organized as follows: Several key concepts and preliminaries are given in Section 2. Section 3 goes into great depth about the presented despeckling process. The experimental results are reported in Section 4. Section 5 draws our paper to a conclusion.

## 2. Notions and preliminaries

In the following part, some notions that will be utilized in the remainder of the paper are introduced. Vectors are indicated as bold lowercase letters, e.g., $\mathbf{x}$; scalars are indicated as non-bold letters, e.g., $a$; and matrices are indicated as bold uppercase letters, e.g., $\mathbf{U}$. Tensors are represented using calligraphic letters, e.g., $\mathscr{A}$. For a third-order tensor $\mathscr{A} \in \mathbb{R}^{n_1 \times n_2 \times n_3}$, the corresponding fast Fourier transformation (FFT) along the 3rd dimension is denoted by $\overline{\mathscr{A}} = fft(\mathscr{A}, [], 3)$. And $A^{(k)}$, which can be expressed by the Matlab notation $\mathscr{A}(:,:,k)$, is used to represented the $k$-th frontal slice of $\mathscr{A}$. Similarly, $\overline{A}^{(k)}$ *respresents t* he $k$-th frontal slice of $\overline{\mathscr{A}}$. The elements of a tensor $\mathscr{A} \in \mathbb{R}^{n_1 \times n_2 \times n_3}$ are denoted as $a_{ijk}$, where $1 \le i \le n_1$, $1 \le j \le n_2$, and $1 \le k \le n_3$. As for a tensor $\mathscr{A}$, the Frobenius norm can be defined as $\left\|\left|\mathscr{A}\right|\right\|_F = \sqrt{\sum_{i=1}^{n_1}\sum_{j=1}^{n_2}\sum_{k=1}^{n_3} a_{ijk}^2}$, and the following property holds $\sum_{i=1}^{n_3}\left\|\left|\overline{A}^{(i)}\right|\right\|_F^2 = \left\|\left|\overline{\mathscr{A}}\right|\right\|_F^2 = n_3\left\|\left|\mathscr{A}\right|\right\|_F^2$ [45]. The block circulant matrix of a third-order tensor $\mathscr{A} \in \mathbb{R}^{n_1 \times n_2 \times n_3}$ is defined in Eq. (1) below:

$$bcirc(\mathscr{A}) = \begin{bmatrix} A^{(1)} & A^{(n_3)} & \cdots & A^{(2)} \\ A^{(2)} & A^{(n_3-1)} & \cdots & A^{(3)} \\ \vdots & \cdots & \ddots & \vdots \\ A^{(n_3)} & A^{(1)} & \cdots & A^{(1)} \end{bmatrix} \tag{1}$$

Two related operators, *MatVec* and *fold*, are shown in Eqs. (2) and (3) below:

$$MatVec(\mathscr{A}) = \begin{bmatrix} A^{(1)} \\ A^{(2)} \\ \vdots \\ A^{(n_3)} \end{bmatrix} \in R^{n_1 n_3 \times n_2} \tag{2}$$

and

$$fold(MatVec(\mathscr{A})) = \mathscr{A} \tag{3}$$

In particular, the block diagonal matrix of a third-order tensor $\overline{\mathscr{A}}$ can be given by the formula defined in Eq. (4):

$$\overline{A} = \left(F_{n_3} \otimes I_{n_1}\right) \cdot bcirc(A) \cdot \left(F_{n_3}^{-1} \otimes I_{n_2}\right) = \begin{bmatrix} \overline{A}^{(1)} & & & \\ & \overline{A}^{(2)} & & \\ & & \ddots & \\ & & & \overline{A}^{(n_3)} \end{bmatrix} \tag{4}$$

where $\overline{A}^{(k)}$ is the $k$-th frontal slice of $\overline{\mathscr{A}}$, and $F_{n_3}$ is the discrete Fourier transformation matrix.

**Definition 1.** [44,45] Given two third-order tensors $\mathscr{A} \in \mathbb{R}^{n_1 \times n_2 \times n_3}$ and $\mathscr{B} \in \mathbb{R}^{n_2 \times n_4 \times n_3}$, the corresponding t-product can be denoted as $\mathscr{A} * \mathscr{B}$, as shown in Eq. (5) below:

$$\mathscr{A} * \mathscr{B} = fold(circ(\mathscr{A}) \cdot MatVec(\mathscr{A})) \in \mathbb{R}^{n_1 \times n_4 \times n_3} \tag{5}$$

According to Eqs. (4) and (5), the t-product of two third-order tensors can be converted to the multiplication of two matrixes in the Fourier domain. Fox instance, $\mathscr{C} = \mathscr{A} * \mathscr{B}$ can be effectively computed as $\overline{C} = \overline{AB}$.

**Definition 2** [44,45]. Let the transpose of a third-order tensor $\mathscr{A} \in \mathbb{R}^{n_1 \times n_2 \times n_3}$ be $\mathscr{A}^T$. Then $\mathscr{A}^T$ is given by Eq. (6) below:

$$\mathscr{A}^T = fold\left(\begin{bmatrix} \left(A^{(1)}\right)^T \\ \left(A^{(n_3)}\right)^T \\ \left(A^{(n_3-1)}\right)^T \\ \vdots \\ \left(A^{(2)}\right)^T \end{bmatrix}\right) \in R^{n_2 \times n_1 \times n_3} \tag{6}$$

**Definition 3.** [44,45] Let $\mathscr{I} \in \mathbb{R}^{n \times n \times n_3}$. If $\mathscr{I}(:,:,k) = 0$ $(k = 2, 3, \cdots, n_3)$ and $\mathscr{I}(:,:,1)$ is the identity matrix, then tensor $\mathscr{I}$ is an identity tensor.

**Definition 4.** [44,45] If $\mathscr{Q}^T * \mathscr{Q} = \mathscr{Q} * \mathscr{Q}^T = \mathscr{I}$, then the tensor $\mathscr{Q} \in \mathbb{R}^{n \times n \times n_3}$ is an orthogonal tensor.

**Definition 5.** [44,45] If each frontal slice of a third-order tensor $\mathscr{A} \in \mathbb{R}^{n_1 \times n_2 \times n_3}$ is a diagonal matrix, then the third-order tensor $\mathscr{A}$ is referred to as the f-diagonal tensor.

**Definition 6.** [45] For a third-order $\mathscr{A} \in \mathbb{R}^{n_1 \times n_2 \times n_3}$, the corresponding tensor nuclear norm (TNN) can be expressed by Eq. (7) as follows:

$$\left\| \mathscr{A} \right|_{\mathrm{TNN}} = \frac{1}{n_3} \sum_{i=1}^{n_3} \left| \left| \overline{\mathrm{A}}^{(i)} \right| \right|_* \tag{7}$$

where $\left\| \cdot \right\|_*$ is the nuclear norm, defined as the sum of the singular values of a matrix.

**Theorem 1.** [44,45] Let $\mathscr{A} \in \mathbb{R}^{n_1 \times n_2 \times n_3}$ be a third-order tensor. Then the formulate defined in Eq. (8) gives its $t$-SVD decomposition form.

$$\mathscr{A} = \mathscr{U} * \mathscr{S} * \mathscr{V}^T \tag{8}$$

where $\mathscr{U} \in \mathbb{R}^{n_1 \times n_1 \times n_3}$ , $\mathscr{V} \in \mathbb{R}^{n_2 \times n_2 \times n_3}$ are two orthogonal tensors defined as in Definition 4, respectively, and the f-diagonal tensor $\mathscr{S} \in \mathbb{R}^{n_1 \times n_2 \times n_3}$ is the decomposition coefficient. According to the Definition 1, the following Eq. (9) is hold

$$\overline{A} = \overline{U}\overline{S}\overline{V}^T \tag{9}$$

**Theorem 2.** [53] Let the SVD of the matrix $Y \in R^{n_1 \times n_2}$ be $Y = USV^T$ , then

$$\widehat{\mathrm{X}} = \mathrm{UD}_\tau(\mathrm{S})\mathrm{V}^\mathrm{T} = \underset{\mathrm{X}}{\operatorname{argmin}} \left\{ \frac{1}{2} \left\| \mathrm{Y} - \mathrm{X} \right\|_\mathrm{F}^2 + \tau \left\| \mathrm{X} \right|_* \right\} \tag{10}$$

where $U \in R^{n_1 \times n_1}$, $V \in R^{n_2 \times n_2}$, $S \in R^{n_1 \times n_2}$, and $\tau > 0$. In Eq. (10), $D_\tau$ is the soft-thresholding operator defined as $D_\tau(t) = max(t - \tau, 0)$.

## 3. The proposed model

In this work, the $t$-SVD notion is adopted to model our method, which is further used to generate speckle suppression results. The first stage of our model consists of three coherent parts: patch grouping, $t$-SVD denoising, and aggregation. In addition, a fractional-

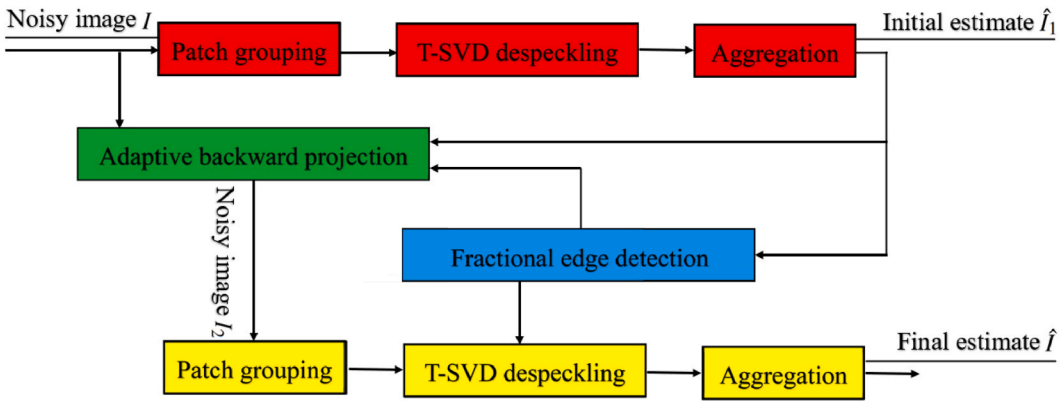


**Fig. 1.** Flowchart of the presented despeckling algorithm.

order diffusion method is used to detect image edges, which are further used to define the feature-guided threshold of singular values and the backward projection parameter of the iterative regularization step. The sequence of steps of the presented despeckling method can be explained by Fig. 1, as shown below.

### 3.1. Patch grouping

The nonlocal mean method [54] is an effective and landmark method in the field of image denoising. And nonlocal self-similarity prior has exhibited impressive performance in image processing. Nonlocal self-similarity means that the image contains many repetitively similar blocks at different scales and spaces. The Euclidean distance, which is commonly utilized in additive Gaussian noise, is used to quantify the similarity of two image patches in the original method. However, the speckle noise in low-coherence images is often regarded as a multiplicative one that follows the Gamma distribution [18]. Therefore, Euclidean distance may not be applicable to measuring the similarity between two low-coherence image patches. To measure the similarity of $Y_i \in R^{n\times n}$ and $Y_c \in R^{n\times n}$, the following similarity criterion [6,38] was adopted, as shown in Eq. (11) below:

$$SC(Y_i, Y_c) = \frac{mean(Y_i \odot Y_c)}{mean((Y_i + Y_c) \odot (Y_i + Y_c))} \tag{11}$$

where $\odot$ depicts the Hadamard product and $mean(\cdot)$ is the function that computes the average of all matrix elements. Eq. (11), Calculated from the gamma distribution [55], is suitable for OCT images. As demonstrated in the literature [6,38], the similarity criteria provided in Eq. (11) has been proven to work well on OCT image despeckling. For a given reference patch $Y_i$, we can find $n_3 - 1$ patches that are most similar to $Y_i$ by using Eq. (11) in a search window of size $W \times W$. And then, these $n_3$ similar patches are stacked into the 3D tensor, denoted as $\mathscr{Y}_i \in \mathbb{R}^{n\times n\times n_3}$.

### 3.2. T-SVD despeckling

In the 3D tensor $\mathscr{Y}_i \in \mathbb{R}^{n\times n\times n_3}$, the reference patch $Y_i$ shares similar features with its $n_3 - 1$ most similar patches. In other words, the 3D tensor $\mathscr{Y}_i$ should have the low-rank property. Therefore, in the logarithmic domain, the noise model can be formulated as $\mathscr{Y}_i = \mathscr{X}_i + \mathscr{N}_i$, here $\mathscr{Y}_i$ is the observed noisy tensor, $\mathscr{X}_i$ is the latent noise-free tensor with low-rank property, and $\mathscr{N}_i$ is the noisy tensor. For the reader to better understand, we are going to substitute $\mathscr{Y}_i$ and $\mathscr{X}_i$ with $\mathscr{Y}$ and $\mathscr{X}$ in the rest of the section, with a small misuse of notation. Our aim is to estimate $\mathscr{X}$ from $\mathscr{Y}$ as accurately as possible. To this end, we minimize the following equation

$$\min_{\mathscr{X}} \frac{1}{2} \left\| \mathscr{Y} - \mathscr{X} \right|_{\mathrm{F}}^2 + \tau \left\| \mathscr{X} \right|_{\mathrm{TNN}} \tag{12}$$

where $\tau = \gamma\sigma\, log\sqrt{n_1 \times n_2 \times n_3}$ and $\sigma$ is the noise variance. By using the property $\sum_{i=1}^{n_3} \left\| \left| \overline{\mathrm{A}}^{(i)} \right|_{\mathrm{F}}^2 = n_3 \right\| \mathscr{A} \left|_{\mathrm{F}}^2 \right.$ and Eq. (7), the above problem (12) can be rewritten as

$$\min_{\overline{\mathrm{X}}} \frac{1}{n_3} \sum_{i=1}^{n_3} \left\{ \frac{1}{2} \left\| \overline{\mathrm{Y}}^{(i)} - \overline{\mathrm{X}}^{(i)} \right|_{\mathrm{F}}^2 + \tau \left\| \overline{\mathrm{X}}^{(i)} \right|_* \right\} \tag{13}$$

Marked the SVD of the matrix $\overline{Y}^{(i)}$ as $\overline{U}^{(i)}\overline{S}^{(i)}\overline{V}^{(i)^T}$, then the estimate matrix of $\overline{X}^{(i)}$ is expressed as $\overline{U}^{(i)}D_\tau(\overline{S}^{(i)})\overline{V}^{(i)^T}$ according to Theorem 2. That is, $\overline{X} = \overline{U}D_\tau(\overline{S})\overline{V}$ is the solution of the problem (13). The matrix $bcirc(\mathscr{X})$ can be obtained by multiplying $F_{n_3}^{-1} \otimes I_{n_1}$ left and $F_{n_3} \otimes$

$I_{n_2}$ right. By folding up $bcirc(\mathscr{X})$, we can obtain the despeckling tensor $\widehat{\mathscr{X}} = \mathscr{U} * \mathscr{S}_\tau * \mathscr{V}^T$. It is worth noting that $\mathscr{U}$, $\mathscr{S}_\tau$ and $\mathscr{V}$ are not necessary to perform *bcirc* operator explicitly and can be obtained by Matlab notation [44], e.g., $\mathscr{U} = ifft(\overline{\mathscr{U}}, [], 3)$, $\mathscr{S}_\tau = ifft(D_\tau(\overline{\mathscr{S}}), [], 3)$, and $\mathscr{V} = ifft(\overline{\mathscr{V}}, [], 3)$.

**Algorithm 1** below describes the pseudo-code for the proposed *t*-SVD despeckling approach.

**Algorithm 1** *t*-SVD despeckling method

**Input:** The noisy tensor $\mathscr{Y}$

**Output:** The despeckling tensor $\widehat{\mathscr{X}}$

**Algorithm:**

1: Compute $\overline{\mathscr{Y}} = fft(\mathscr{Y}, [], 3)$;

2: **for** $i = 1, \cdots, \left\lceil \frac{n_3+1}{2} \right\rceil$ **do**

3: $[\overline{U}^{(i)}, \overline{S}^{(i)}, \overline{V}^{(i)}] = SVD(\overline{Y}^{(i)})$,

4: $\overline{W}^{(i)} = \overline{U}^{(i)} D_\tau(\overline{S}^{(i)}) \overline{V}^{(i)^T}$,

5: **end for** 6: **for** $i = \left\lceil \frac{n_3+1}{2} \right\rceil + 1, \cdots, n_3$ **do**

7: $\overline{W}^{(i)} = conj(\overline{W}^{(n_3-i+2)})$;

8: **end for** 9: Return $\widehat{\mathscr{X}} = ifft(\overline{\mathscr{W}}, [], 3)$.

### 3.3. Aggregation

By scanning all patches of OCT images in an overlapping fashion, each corresponding noisy 3D tensor can be processed by the above *t*-SVD despeckling method. Then, the whole OCT image can be reconstructed by writing the filtered patches back to their original locations. However, the overlapping fashion may make a single image patch belong to more than one tensor. That is, multiple estimates of each image patch may be obtained. To deal with this problem, an aggregation strategy is applied to filtered 3D tensors. Specifically, the final estimated $\widehat{I}(i)$ of $I(i)$ can be computed using Eq. (14) below, and $I(i)$ denotes the intensity value at pixel $i$.

$$\widehat{I}(i) = \frac{\sum_{j=1}^{V} \sum_{k=1}^{K_j} \mathscr{T}_j^k(i)}{\sum_{j=1}^{V} K_j} \tag{14}$$

where $V$ represents the quantity of third-order tensors that include pixel $i$, $K_j$ depicts the quantity of image patches that include the pixel $i$ in the given third-order tensor $\mathscr{T}_j$. At the pixel $i$ in the $k$-th patch of the third-order tensor $\mathscr{T}_j$, the corresponding intensity value is denoted by $\mathscr{T}_j^k(i)$.

### 3.4. Fractional-order edge detection

As previously mentioned, the parameter of the backward projection and the setting of the threshold value are critical for obtaining speckle suppression and detail preservation results. As point out in Ref. [56], fractional-order differentiation can boost the high-frequency components, enhance the medium-frequency components, and nonlinearly retain the low-frequency components, such as the fine features of the image. To get the edges of noisy input images, we proposed a novel edge detection approach by using a fractional-order differentiation-based diffusion equation. Moreover, the detected edge information is further applied to define the feature-guided threshold of singular values and the backward projection parameter of the iterative regularization step. To be more specific, the fractional-order diffusion equation established in Eq. (15) below is utilized for filtering the noisy input image $I$. After that, an adaptive order-based edge indicator is defined to extract the edges of the filtered result.

$$\frac{\partial I}{\partial t} = -D_x^{\alpha*}\left(g(DC) D_x^\alpha I\right) - D_y^{\alpha*}\left(g(DC) D_y^\alpha I\right) \tag{15}$$

where $\alpha \in (1, 2)$, the diffusivity function $g(DC)$ is defined as $exp(-DC/100)$, and the difference curvature $DC$ is expressed in Eq. (16) below:

$$\mathrm{DC} = \left\| \mathrm{I}_{\eta\eta} | - | \mathrm{I}_{\xi\xi} \right\| \tag{16}$$

and $I_{\eta\eta}$ and $I_{\xi\xi}$ are depicted in Eqs. (17) and (18):

$$I_{\eta\eta} = \frac{I_x^2 I_{xx} + 2 I_x I_y I_{xy} + I_y^2 I_{yy}}{I_x^2 + I_y^2} \tag{17}$$

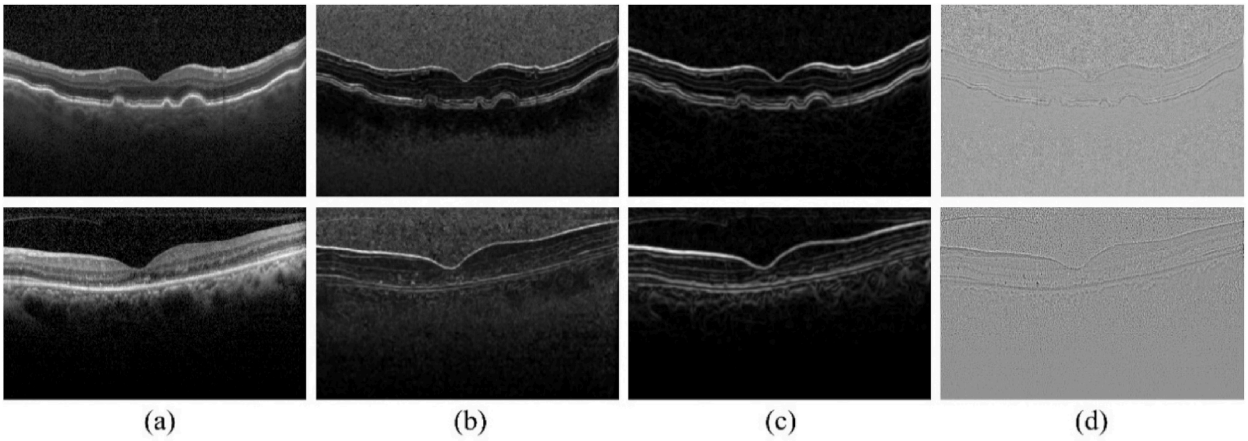


**Fig. 2.** Comparisons with LoG filter. (a) Noisy images; (b) Edges obtained by Eq. (25) without smoothing; (c) Edges obtained by Eq. (25) with smoothing by Eq. (15); (d) Edges obtained by the LoG filter.

$$I_{\xi\xi} = \frac{I_y^2 I_{xx} - 2I_x I_y I_{xy} + I_x^2 I_{yy}}{I_x^2 + I_y^2} \tag{18}$$

And first-order derivatives $I_x$ and $I_y$ can be effectively computed by the following central difference scheme, as shown in Eq. (19) below:

$$I_x(i,j) = \frac{I(i+1,j) - I(i-1,j)}{2} \ and \ \ I_y(i,j) = \frac{I(i,j+1) - I(i,j-1)}{2} \tag{19}$$

and $I_{xx}$ and $I_{yy}$ can be computed similarly. And the fractional-order derivatives can be computed by the Grünwald-Letnikov definition [57], as shown in Eq. (20) below:

$${}_{t_0}^{G}D_t^{\alpha} s(t) = \lim_{h\to 0} \frac{1}{h^{\alpha}} \sum_{j=0}^{[(t-t_0)/h]} w_j^{\alpha} s(t-jh) \tag{20}$$

where $w_j^{\alpha} = (-1)^j \binom{\alpha}{j}$ and $\binom{\alpha}{j} = \frac{\alpha(\alpha-1)\cdots(\alpha-j+1)}{j!}$. Taking the step size $h = 1$ and $n = [t - t_0]$, then fractional-order derivatives $D_x^{\alpha}$ and $D_y^{\alpha}$ can be approximated numerically using the formulas in Eqs. (21) and (22) below:

$$D_x^{\alpha} I(x,y) \approx \sum_{j=0}^{n} w_j^{\alpha} I(x-j,y) \tag{21}$$

$$D_y^{\alpha} I(x,y) \approx \sum_{j=0}^{n} w_j^{\alpha} I(x,y-j) \tag{22}$$

And the conjugates $D_x^{\alpha*}$ and $D_y^{\alpha*}$ [56] are represented in Eqs. (23) and (24):

$$D_x^{\alpha*} I(x,y) \approx \sum_{j=0}^{n} w_j^{\alpha} I(x+j,y) \tag{23}$$

$$D_y^{\alpha*} I(x,y) \approx \sum_{j=0}^{n} w_j^{\alpha} I(x,y+j) \tag{24}$$

As pointed out in Ref. [58], $DC$ has a high value around the edges of the image and a low value in flat areas. Therefore, we can conclude the following behaviors of Eq. (15): (1) For flat regions, the value of $DC$ is small, so the diffusivity function $g(DC)$ is large. Therefore, Eq. (15) can effectively smooth the flat regions. (2) For edges, the value of $DC$ is large, so the diffusivity function $g(DC)$ is small. Therefore, Eq. (15) can preserve important image edges. When we obtain the smoothed image $\widehat{I}$, the following equation (25) can be utilized to detect the edges of OCT images.

$$E(x,y)=\frac{1}{25}\sum_{(s,t)\in N}\frac{\left|(\widehat{I}(s,t))^{b(x,y)}-(c(x,y))^{b(x,y)}\right|}{c(x,y)+\varepsilon} \tag{25}$$

where $c(x,y)$ denotes the mean of the intensities that are located in the window $N$ of size $5\times 5$, and $\varepsilon$ is a small positive constant. In practice, the value of $b$ should be very carefully set. If $b$ is large, then $E(x,y)$ is susceptible to interference from noise. If $b$ is large, then $E(x,y)$ does not detect smaller dynamic changes, e.g., weak edges of OCT images. To tackle this problem, an adaptive order function $b(x,y)$ is defined in Eq. (26) below:

$$b(x,y)=\frac{2*(1+T)}{1+\sqrt{I_x^2+I_y^2}} \tag{26}$$

here $T$ is the maximum value of $\sqrt{I_x^2+I_y^2}$. In flat regions, $\sqrt{I_x^2+I_y^2}\approx 0$, so $b(x,y)\approx 1$. And at edges, $\sqrt{I_x^2+I_y^2}\approx T$, so $b(x,y)\approx 2$. Therefore, the proposed adaptive order function helps the edge detection function capture more reliable edges. As demonstrated in Fig. 2(a)-(d), the edge detection method proposed in this paper can obviously obtain more realistic edge information than the Laplacian of Gaussian (LoG) filter.

### 3.5. Adaptive backward projection

As mentioned previously, the iterative regularization strategy based on the backward projection method is an often-used technique to increase the despeckling performance of methods. In this study, we follow this idea. Before the next processing, the input noisy image is regenerated using the formula defined in Eq. (27):

$$I_2=\widehat{I}_1+\eta(I-\widehat{I}_1) \tag{27}$$

where $\widehat{I}_1$ represents the filtered image of $I$ after the first denoising step, $I-\widehat{I}_1$ is the called method noise, and $I_2$ is the regenerated noisy image according to Eq. (27). The projection parameter $\eta\in(0,1)$ is often established as a fixed constant without taking into account the inherent feature properties, e.g., edge information. To address this issue, the projection parameter $\eta$ is redefined by using the edge information of images. The main motivation behind this is that the lost information $I-\widehat{I}_1$ contains not only noise but also image edges. Therefore, the lost image edges should be reused. In addition, $\eta$ should be small in flat regions so that these regions can be well smoothed. On the contrary, $\eta$ should be large at the image edges so that image edges can be well preserved. Therefore, we define a new projection parameter based on image edges, as shown in Eq. (28) below:

$$\eta=\begin{cases}\varepsilon\ , & E=E_{min}\\ \dfrac{E-E_{min}}{E_{max}-E_{min}}, & E_{min}<E<E_{max}\\ 1-\varepsilon, & E=E_{max}\end{cases} \tag{28}$$

where $E_{max}$ is the maximum value of $E$, which is obtained by Eq. (25), and the corresponding minimum value is represented by $E_{min}$. $\varepsilon$ is a small positive constant. Obviously, the defined backward projection parameter $\eta$ is proportional to the value of the edge image $E$ and takes a value in the interval $(0,1)$. In addition, $\eta$ takes a small value in flat regions and a large value at image edges. Consequently, the lost information $I-\widehat{I}_1$ can be reused according to image features. That is, $I-\widehat{I}_1$ is barely used in flat regions. Hence, flat regions can be further smoothed. And more lost information $I-\widehat{I}_1$ is reused at image edges. Hence, the edges of OCT images can be well preserved. When the input noisy image is obtained according tomEq. (27), the corresponding noise variance $\sigma$ is updated using the formula in Eq. (29) below:

$$\widehat{\sigma}=\lambda\sqrt{\sigma^2-mean\left(\left\|I-I_2\right\|_F^2\right)} \tag{29}$$

here, the noise variance $\widehat{\sigma}$ can be re-estimated by Eq. (29) and is regulated by the scaling factor $\lambda$ .On the other hand, the noise variance $\sigma$ of $I$ can be estimated by the method in Ref. [59].

### 3.6. Feature-guided threshold

The threshold parameter $\tau$ in Eq. (12) is used to control the smoothness of the filtered image. If $\tau$ is too small, then more noise will be retained in the filtered images. If $\tau$ is too large, an over-smoothed image will be obtained. To deal with this problem, we propose an adaptive threshold parameter that is constructed by using the edge feature. The threshold parameter of the second denoising stage is defined as illustrated in Eq. (30):

$$\tau_2(x,y)=\frac{\gamma\widehat{\sigma}log\sqrt{n_1\times n_2\times n_3}}{\varepsilon+|ME(x,y)|} \tag{30}$$

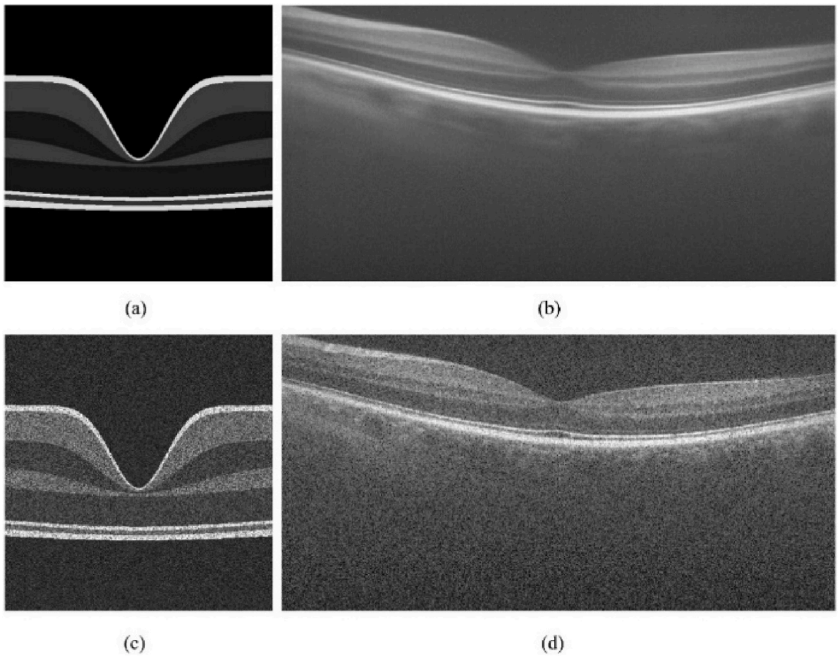


**Fig. 3.** Two synthetic images used in this work. (a) Gaussian function-generated speckle-free image according the method proposed in Ref. [20]; (b) Speckle-free image randomly selected from the dataset [32]; (c) Matlab function *imnoise*-generated speckle noisy image according to Fig. 3(a); (d) Speckle noisy image of (b).

where $\varepsilon$ is a small positive constant, $\gamma$ is a regulation parameter, and $\hat{\sigma}$ is the re-estimated noise variance defined in Eq. (29). $ME(x,y)$ is the average value of $E(x,y)((x,y) \in \Omega)$, and the set $\Omega$ collects the central points of all the frontal slices included in $\mathscr{Y}$. Taking $ME(x,y)$ instead of $E(x,y)$ is intended to reduce the effect of spurious edges. It is easy to find that $ME(x,y)$ takes a larger value in the vicinity of edges and a smaller value in flat regions. Since the defined $\tau_2(x,y)$ is inversely proportional to $ME(x,y)$, a lesser shrinkage will result for these tensors with more image details; otherwise, a higher shrinkage will result. Therefore, the defined threshold parameter above can effectively help our model suppress speckle noise and maintain the feature detail of OCT images.

**Algorithm 2** below describes the pseudo-code for the presented speckle noise reduction method.

**Algorithm 2** The presented speckle noise reduction method

**Input:** The original noisy image $I$
**Output:** The speckle suppression image $\widehat{I}$
**Algorithm:**
1: **The first stage:**
2: Scanning all patches of the image $I$ in an overlapping fashion;
3: **for** each reference patch $Y_i$ **do**
4: Find the corresponding 3D noise tensor $\mathscr{Y}$ according to Eq. (11).
5: Obtain the estimation $\widehat{\mathscr{X}}$ by Algorithm 1;
6: **end for** 7: Aggregate all $\widehat{\mathscr{X}}$ to form speckle suppression image $\widehat{I}_1$ according to Eq. (14);
8: **The second stage:**
9: Compute the image edge $E$ by Eq. (25);
10: Update the noisy image $I_2$ by Eq. (27);
11: Scanning all patches of the image $I_2$ in an overlapping fashion;
12: **for** each reference patch $Y_i$ **do**
13: Find the corresponding 3D noise tensor $\mathscr{Y}$ according to Eq. (11).
14: Compute the threshold parameter $\tau_2$ according to Eq. (30);
15: Obtain the estimation $\widehat{\mathscr{X}}$ by Algorithm 1;
16: **end for** 17: Aggregate all $\widehat{\mathscr{X}}$ to form speckle suppression image $\widehat{I}$ according to Eq. (14);
18: **Return** The speckle suppression image $\widehat{I}$.

## 4. Experimental results

Both real and synthetic OCT images are utilized to illustrate the speckle suppression effectiveness of our model, which will be further compared to some of the models with high performance, such as TGV [20], PNLM [30], SBSDI [32], FoSVS [37], DnCNN [43],

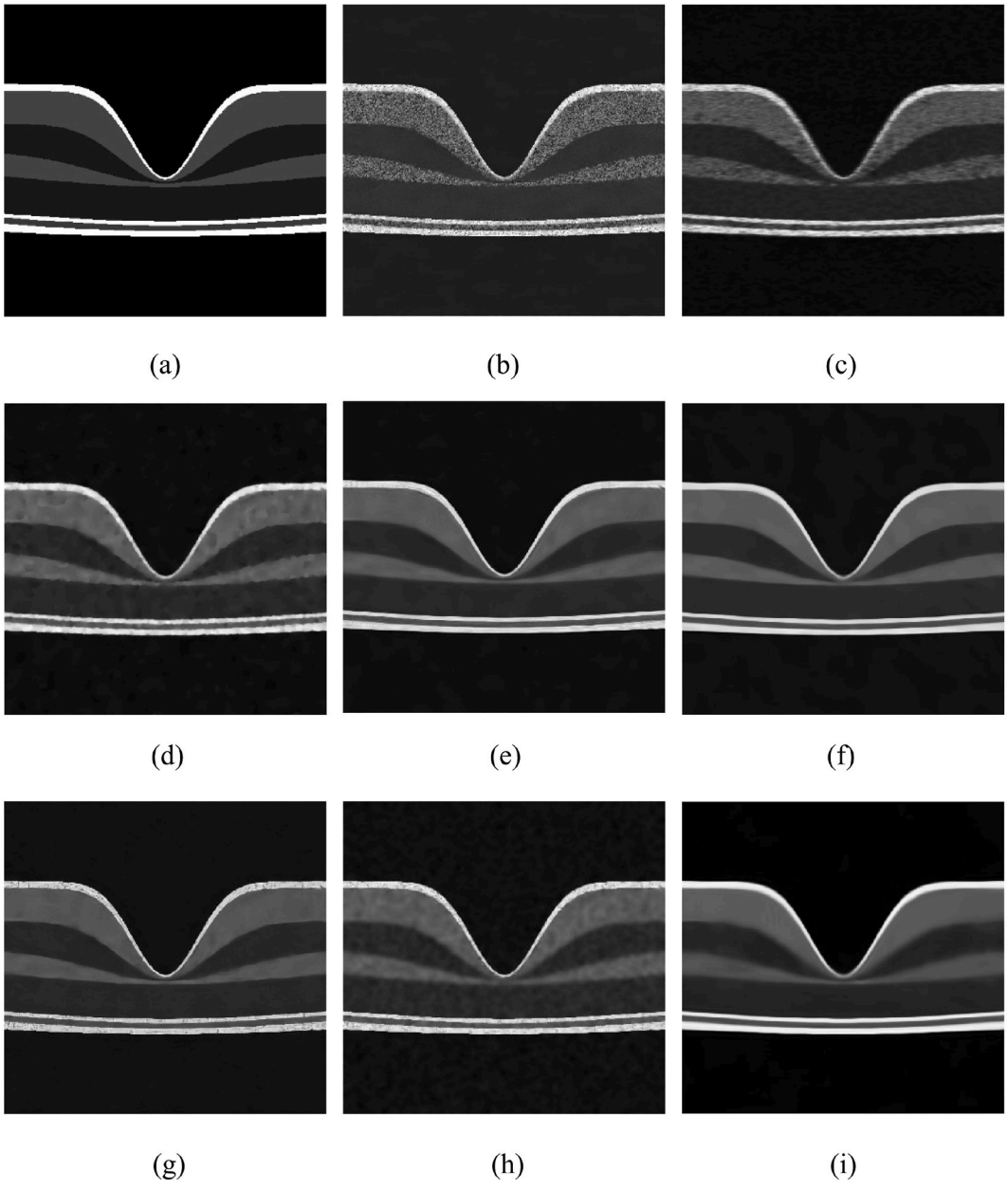


**Fig. 4.** Speckle suppression results of Fig. 3(c). (a) Speckle-free image; (b)–(i) Despeckling results respectively obtained by PNLM [30], SBSDI [32], TGV, FoSVS [20], WGLRR [39], DnCNN [43], CWDL [36], and our method.

and CWDL [36]. If not otherwise specified, the parameters of the method in this paper remain fixed and are as follows: $n = 11$, $n_3 = 60$, $\gamma = 7$ and $\lambda = 0.6$. For the sake of fairness, the comparison techniques' parameters are kept at the fixed values indicated in the references.

For the purpose of demonstrating the speckle suppression performance of our model, we will evaluate and analyze the despeckling results using several quantitative metrics, which are listed below: Edge preservation index (EPI) [60,61], Peak signal-to-noise ratio (PSNR) [6], Equivalent number of looks (ENL) [18,61], Structural similarity index measure (SSIM) [42], Contrast-to-noise ratio (CNR) [5], and Cross correlation (XCOR) [25]. Let $\widehat{y} \in R^{W \times H}$ be the despeckling result and $y$ be the corresponding reference image, then these metrics are represented below.

PSNR defined in Eq. (31) measures the difference in image intensity between $y$ and $\widehat{y}$, and a high PSNR value indicates an excellent reconstruction result.

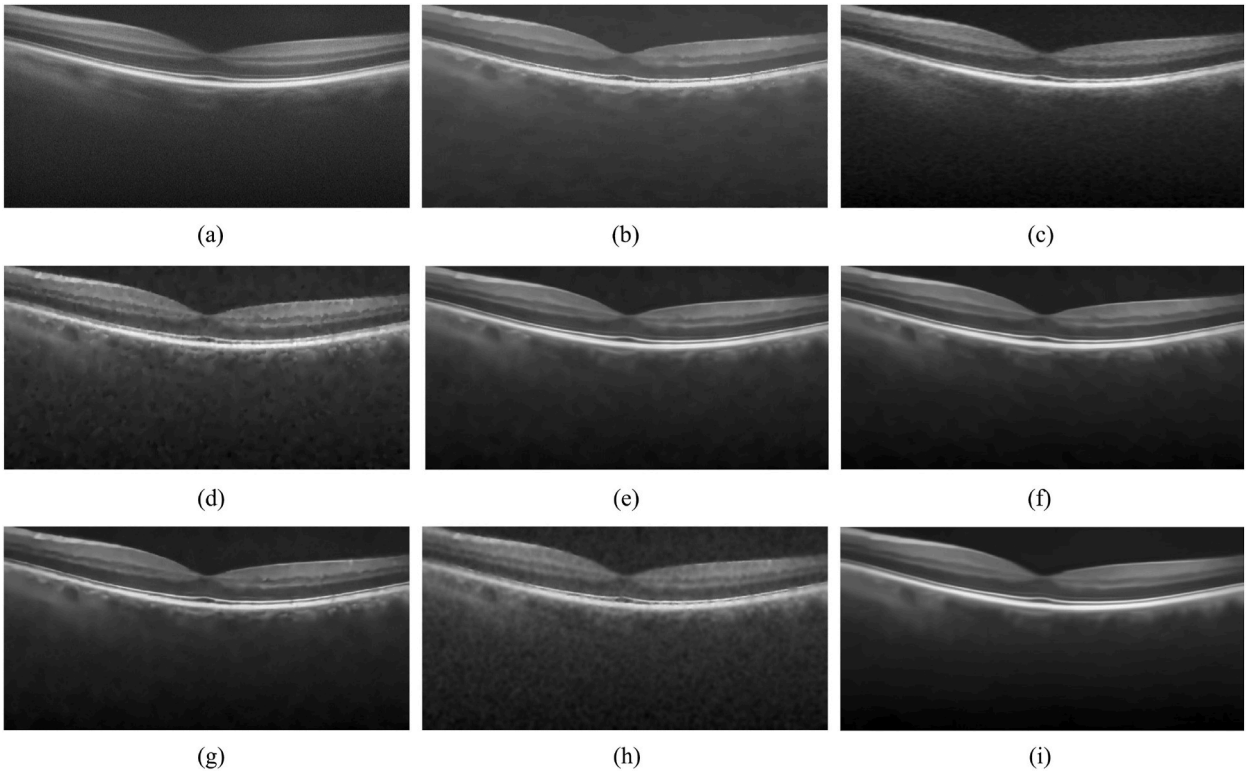


**Fig. 5.** Speckle suppression results of Fig. 3(d). (a) Speckle-free image; (b)–(i) Despeckling results respectively obtained by PNLM [30], SBSDI [32], TGV, FoSVS [20], WGLRR [39], DnCNN [43], CWDL [36], and our method.

**Table 1**
Metrics about Fig. 3(c) for all methods.

| Metric | PNLM | SBSDI | TGV | FoSVS | WGLRR | DnCNN | CWDL | Ours |
|---|---|---|---|---|---|---|---|---|
| PSNR | 17.20802 | 21.7717 | 1.1838 | 22.0129 | 21.8148 | 21.6844 | 21.4593 | **23.5891** |
| SSIM | 0.1836 | 0.3012 | 0.3434 | 0.3534 | 0.3569 | 0.3544 | 0.3339 | **0.5518** |
| XCOR | 0.8716 | 0.9367 | 0.9457 | 0.9535 | 0.9457 | 0.9408 | 0.9451 | **0.9709** |
| EPI | 0.3390 | 0.4453 | 0.7415 | **0.7883** | 0.7203 | 0.7695 | 0.7812 | 0.7432 |

**Table 2**
Averaged metrics about 18 images in the dataset [32] for all methods.

| Metric | PNLM | SBSDI | TGV | FoSVS | WGLRR | DnCNN | CWDL | Ours |
|---|---|---|---|---|---|---|---|---|
| PSNR | 27.5466 | 28.3132 | 19.9145 | 28.2389 | 28.2891 | 28.0918 | 27.8272 | **28.3707** |
| SSIM | 0.6865 | 0.6890 | 0.6081 | 0.6962 | 0.6965 | 0.6909 | 0.6811 | **0.6975** |
| XCOR | 0.9931 | 0.9937 | 0.9641 | 0.9934 | 0.9935 | 0.9932 | 0.9931 | **0.9938** |
| EPI | 0.3255 | 0.3672 | 0.2620 | 0.3659 | 0.3648 | 0.3566 | 0.3684 | **0.3812** |

$$PSNR = 10log_{10}\left(\frac{255^2}{\sum_{i=1}^{W}\sum_{i=1}^{H}\left(\hat{y}(i,j) - y(i,j)\right)^2}\right) \tag{31}$$

SSIM evaluates the structural similarities between the reference image and the recovered one and accounts for the changes in contrast, luminance, and local structure of the images. And SSIM is given by Eq. (32) below.

$$SSIM = \frac{\left(2\mu_y\mu_{\hat{y}} + c_1\right)\left(2\sigma_{y\hat{y}} + c_2\right)}{\left(\mu_y^2 + \mu_{\hat{y}}^2 + c_1\right)\left(\sigma_y^2 + \sigma_{\hat{y}}^2 + c_2\right)} \tag{32}$$

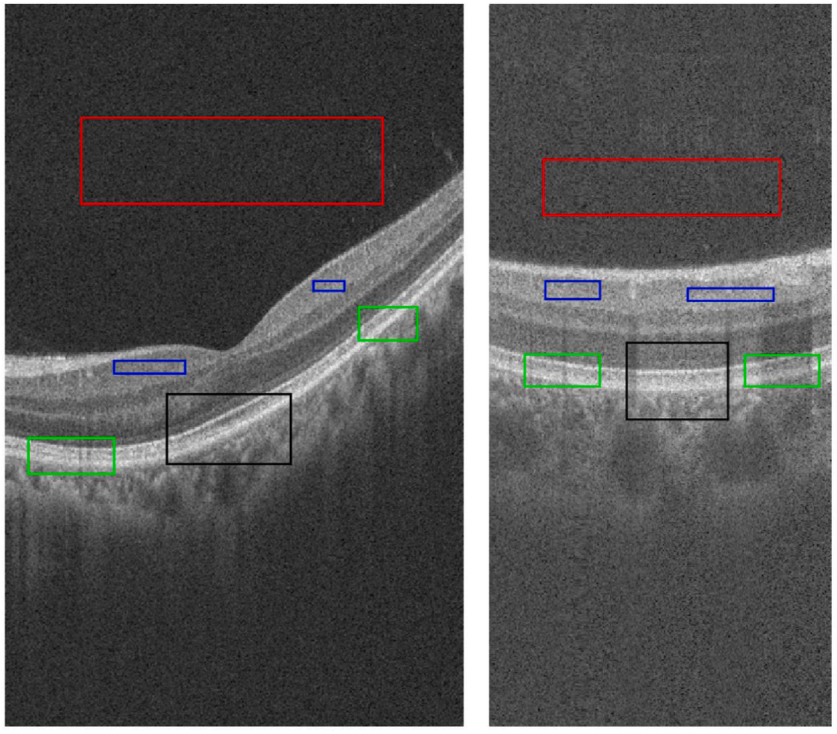


**Fig. 6.** Two real OCT images randomly selected from the dataset [62]. The regions with blue borders are used to calculate ENL, which accounts for the flat regions' smoothness. The foreground and background regions, used to calculate the CNR defined in Eq. (36), are indicated by red borders and green borders. The areas with black borders are two regions of interest, which will be enlarged to better observe the ability of the methods for speckle noise suppression.

here, $\mu_y$ and $\mu_{\hat{y}}$ are the means of the noisy image $y$ and the filtered image $\hat{y}$, respectively. $\sigma_y$ and $\sigma_{\hat{y}}$ are the standard deviations of the corresponding images, respectively. $\sigma_{y\hat{y}}$ means the cross-covariance between $y$ and $\hat{y}$. $c_1$ and $c_2$ are two constants defaulted to 0.01 and 0.03, which are used to maintain numerical stability. SSIM lies in $[0,1]$, and a higher SSIM value means an excellent reconstruction result.

XCOR is used to indicate how similar $y$ and $\hat{y}$ are to each other, and a larger value means a stronger similarity. XCOR is given by Eq. (33) below.

$$\mathrm{XCOR} = \frac{\sum_{i=1}^{W}\sum_{i=1}^{H}\hat{y}(i,j)\cdot y(i,j)}{\sqrt{\left[\sum_{i=1}^{W}\sum_{i=1}^{H}\left|\hat{y}(i,j)\right|^2\right]\cdot\left[\sum_{i=1}^{W}\sum_{i=1}^{H}\left|y(i,j)\right|^2\right]}} \tag{33}$$

EPI accounts for the edge-preserving capability of the algorithm, as shown in Eq. (34).

$$EPI = \frac{\sum(\Delta y - \overline{\Delta y})(\Delta\hat{y} - \overline{\Delta\hat{y}})}{\sqrt{\sum(\Delta y - \overline{\Delta y})^2\cdot\sum(\Delta\hat{y} - \overline{\Delta\hat{y}})^2}} \tag{34}$$

here, $\Delta$ is the Laplace operator of size $3\times 3$. $\overline{y}$ is the mean of $y$. EPI lies in $[0,1]$, and the higher value means that more fine details (edges) are preserved in the filtered images.

ENL is most commonly used in speckle suppression and is utilized to evaluate the flat regions' smoothness, As shown in Eq. (35).

$$ENL = \frac{\mu_{roi}^2}{\sigma_{roi}^2} \tag{35}$$

where *roi* represents the region of interest in the speckle suppression result $\hat{y}$. $\mu_{roi}$ stands for the mean of *roi*, and $\sigma_{roi}$ represents the standard deviation of *roi*. And a larger ENL value means that the approach is more capable of smoothing in homogeneous areas.

CNR defined in the following equation (36) measures the contrast between the background and foreground areas.

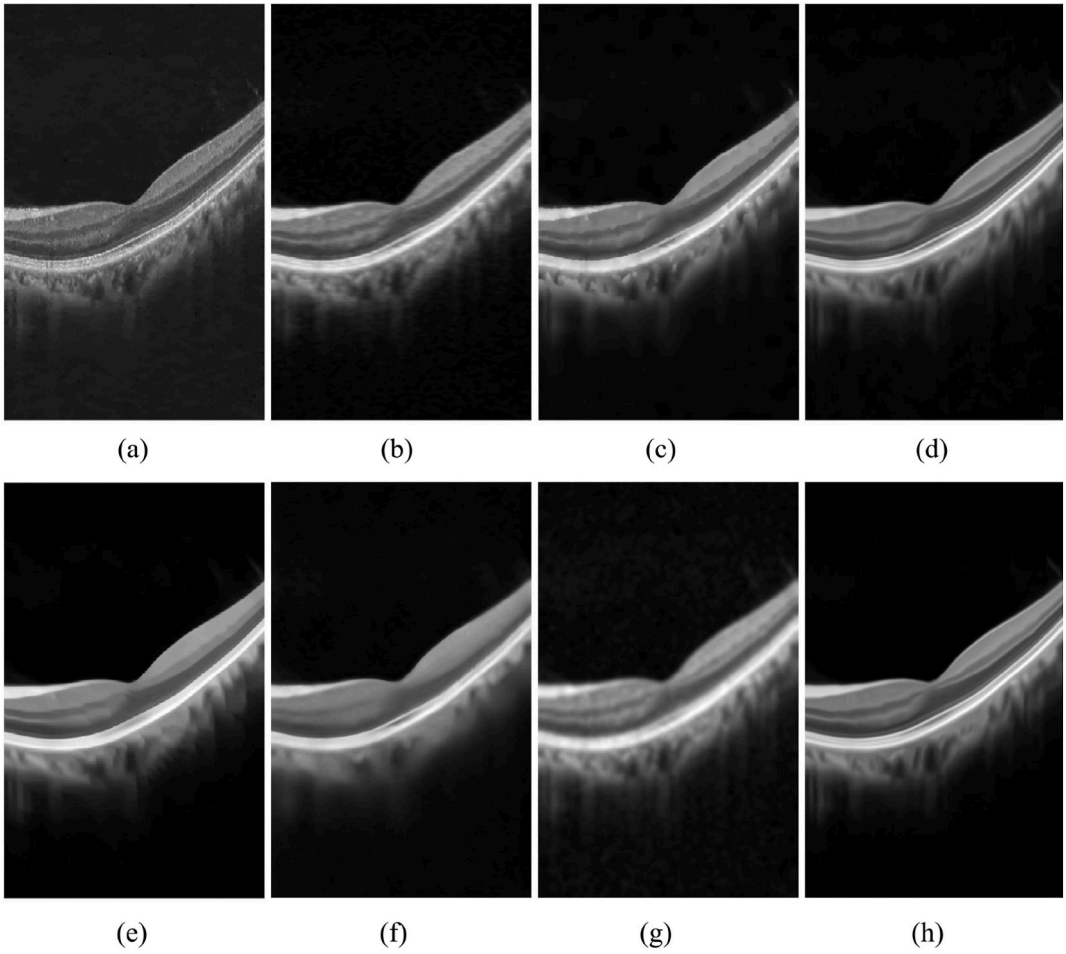


**Fig. 7.** Speckle suppression images of Fig. 6(b). (a)–(h) Despeckling images respectively generated by PNLM [30], SBSDI [32], TGV, FoSVS [20], WGLRR [39], DnCNN [43], CWDL [36], and our method.

$$CNR = \frac{|\mu_f - \mu_b|}{\sqrt{0.5\left(\sigma_f^2 + \sigma_b^2\right)}} \tag{36}$$

here the subscript $b$ stands for background, and the subscript $f$ stands for background. $\sigma_f$ ($\sigma_b$) represents the standard deviation of the corresponding area. In addition, $\mu_f$ ($\mu_b$) is the mean of the corresponding area. It should be noted that the calculation of EPI and CNR does not require the reference image and is most commonly used in real OCT images. And a larger value means better speckle suppression results.

### 4.1. Results on synthetic images

Reference OCT images are generally not available in practice. To illustrate how well the presented model reduces speckle noise, two synthetic OCT images depicted in Fig. 3 are used. The first synthetic image is generated by the Gaussian simulation method used in Ref. [30], and the generated speckle-free image is displayed in Fig. 3(a). In order to obtain a speckle noise-contaminated image, we use the Matlab function *imnoise* to add speckle noise to Fig. 3(a), and the density of noise is set to 0.2. Fig. 3(c) gives the result. The dataset [32] contains 18 synthetic images; Fig. 3(b) is a randomly selected image. In addition, the noisy image corresponding to Fig. 3(b) is presented in Fig. 3(d).

Fig. 4(a)-(i) show the filtered images of all methods corresponding to Fig. 3(c), and the results related to Fig. 3(d) are shown in Fig. 5(a)-(i). It can be observed that a lot of noise is retained in the results of TGV, SBSDI, PNLM, and CWDL. By contrast, WGLRR, FoSVS, DnCNN, and the proposed method not only provide more pleasant visual results but also preserve image edge information well. Table 1 and Table 2, which include the PSNR, SSIM, XCOR, and EPI of all methods, also indicate the well-performing speckle suppression of our method. As shown in Table 1, the method in this work achieves relatively good results in terms of these metrics for Fig. 3

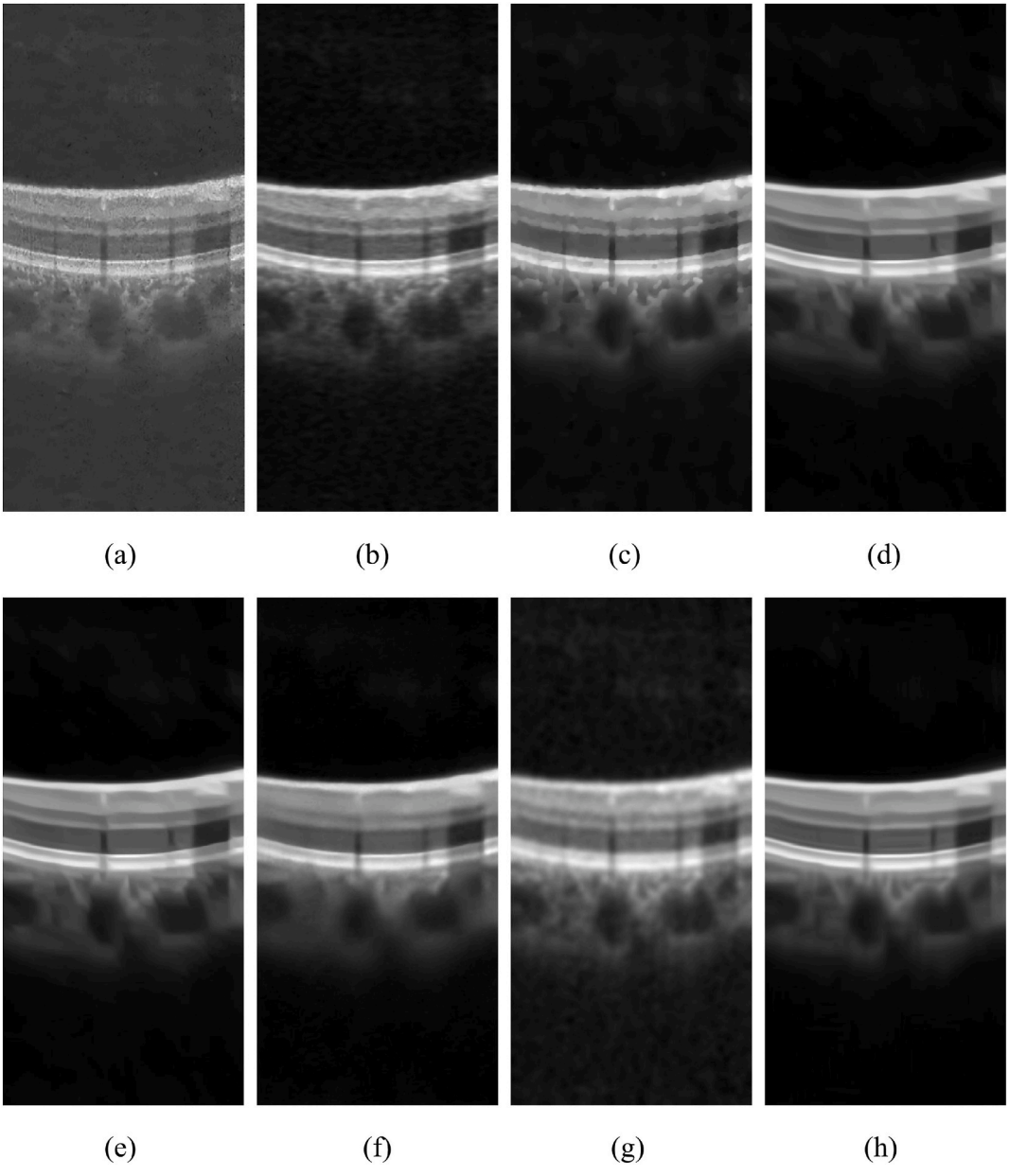


**Fig. 8.** Speckle suppression images of Fig. 6(b). (a)–(h) Despeckling images respectively generated by PNLM [30], SBSDI [32], TGV, FoSVS [20], WGLRR [39], DnCNN [43], CWDL [36], and our method.

(c). Fig. 5 gives the speckle suppression results of different methods for Fig. 3(d). As mentioned above, Fig. 3(b) is a randomly selected image from the dataset [32]. The averaged metrics of all images may better reflect the speckle suppression performance of our method. In terms of these metrics, our method yields superior numerical outcomes, as indicated by Table 2.

### *4.2. Results on real images*

Experiments on synthetic images are not sufficient to prove the superiority of our method. To further illustrate the capabilities of our method in terms of speckle noise removal, we adopt the real OCT dataset [62] in the following subsection. For specific details related to this dataset, we suggest the reader consult the literature [62]. Due to the limitation of space, two images from the real OCT dataset [62] are chosen at random, and they are presented in Fig. 6(a) and (b). And the speckle suppression results of all methods are presented in Fig. 7(a)-(h) and Fig. 8(a)-(h), which give a visual comparison. To better observe methods' ability to retain the details of OCT images, close-ups of regions with blue borders in Fig. 6 are displayed in Fig. 9(a)-(h) and Fig. 10(a)-(h), respectively. It is easy to find that severe speckle noise is present in the two selected OCT images. And TGV, SBSDI, PNLM, and CWDL can provide a relatively

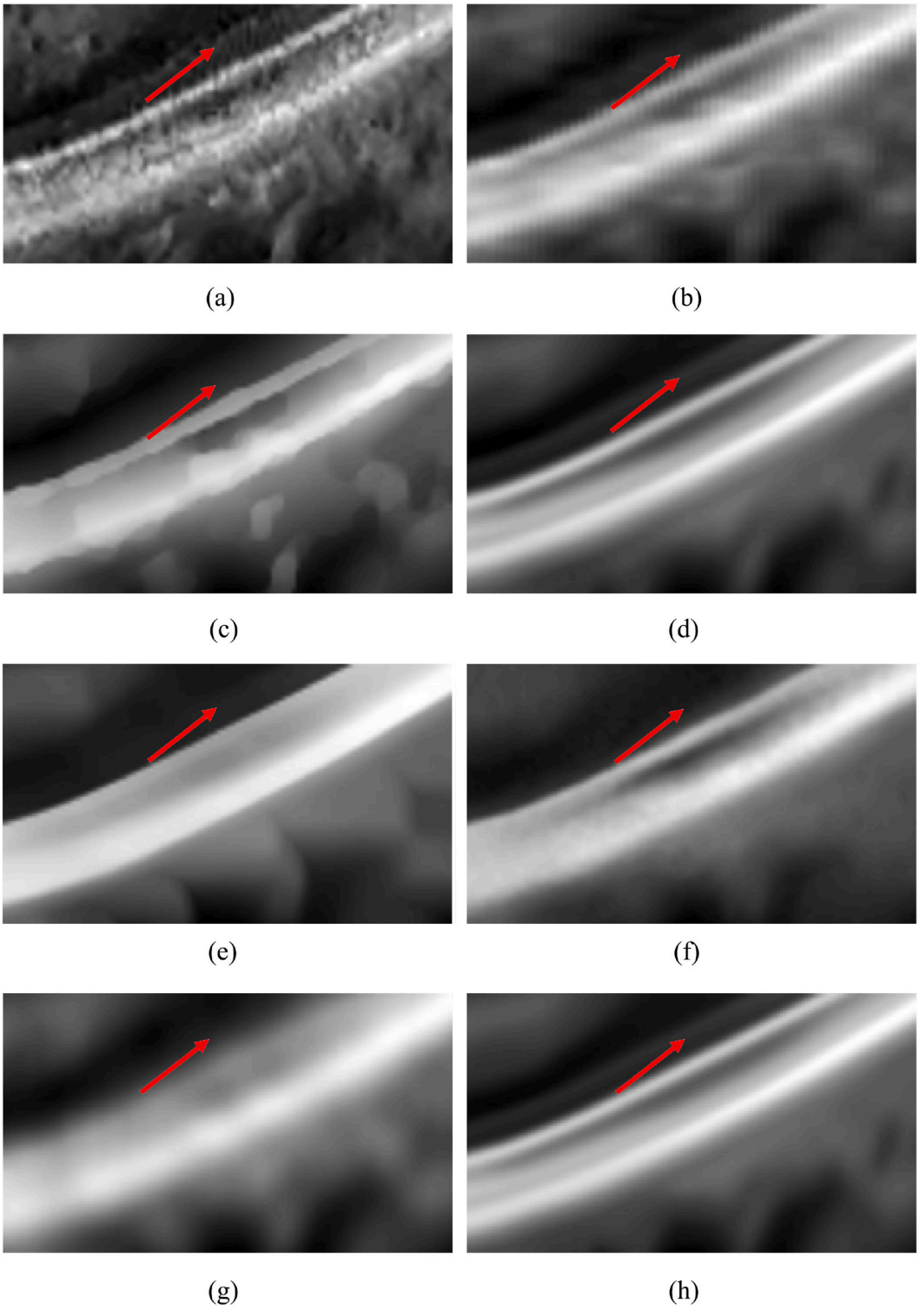


**Fig. 9.** Close-ups of regions with blue borders in Fig. 6(a). (a)–(h) Despeckling results respectively obtained by PNLM [30], SBSDI [32], TGV, FoSVS [20], WGLRR [39], DnCNN [43], CWDL [36], and our method.

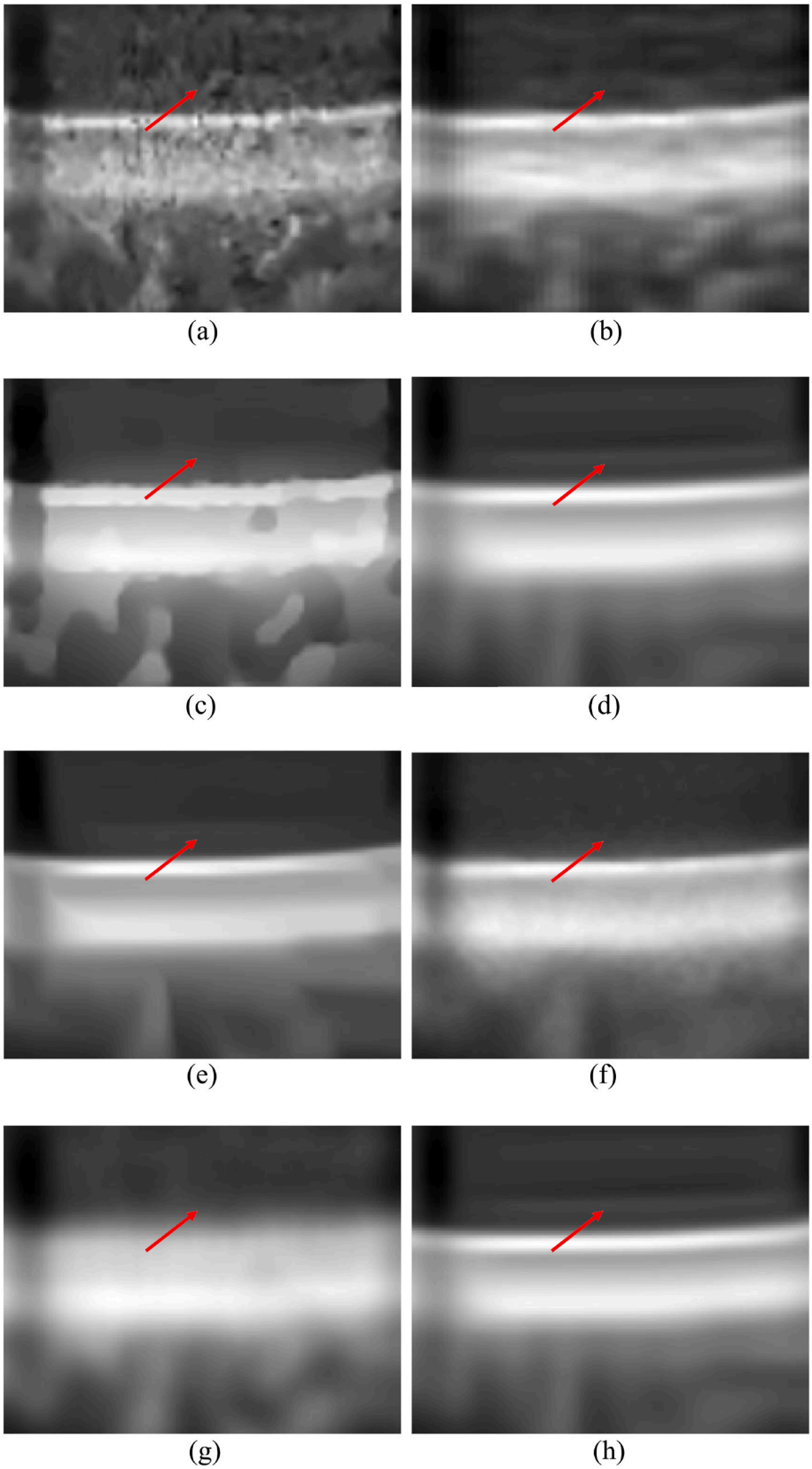


(caption on next page)

**Fig. 10.** Close-ups of regions with blue borders in Fig. 6(b). (a)–(h) Despeckling results respectively obtained by PNLM [30], SBSDI [32], TGV, FoSVS [20], WGLRR [39], DnCNN [43], CWDL [36], and our method.

**Table 3**
Metrics about Fig. 6(a) for all methods.

| Metric | PNLM | SBSDI | TGV | FoSVS | WGLRR | DnCNN | CWDL | Ours |
|---|---|---|---|---|---|---|---|---|
| Q | 6.0878 | 9.4976 | 10.0164 | 13.2204 | 11.8548 | 8.3794 | 9.1599 | **13.4917** |
| ENL | 566.7953 | 711.9132 | 631.3823 | 812.2935 | 892.2207 | 851.5683 | 613.6817 | **932.1125** |
| CNR | 4.0294 | 4.5955 | 4.5119 | 4.3545 | 4.4737 | 4.6519 | 4.3705 | **4.7522** |

**Table 4**
Metrics about Fig. 6(b) for all methods.

| Metric | PNLM | SBSDI | TGV | FoSVS | WGLRR | DnCNN | CWDL | Ours |
|---|---|---|---|---|---|---|---|---|
| Q | 4.6111 | 12.2879 | 10.2546 | 13.0845 | 12.8771 | 8.7428 | 8.9607 | **13.5620** |
| ENL | 204.8645 | 316.2581 | 377.8718 | 466.2603 | 551.5379 | 451.1828 | 390.5915 | **917.1556** |
| CNR | 4.2726 | 4.9217 | 5.0524 | 4.9578 | 5.1153 | 5.2151 | 4.9745 | **5.2246** |

**Table 5**
Computational cost (seconds) for all methods.

| Figures | PNLM | SBSDI | TGV | FoSVS | WGLRR | DnCNN | CWDL | Ours |
|---|---|---|---|---|---|---|---|---|
| Fig. 3(c) (516 × 500) | 20.23 | 7.00 | 8.66 | 88.23 | 83.67 | 4.66 | 5.01 | 53.98 |
| Fig. 3(d) (450 × 900) | 11.14 | 11.91 | 19.45 | 133.36 | 130.06 | 7.33 | 20.59 | 87.97 |
| Fig. 6(a) (600 × 400) | 19.93 | 4.84 | 11.32 | 84.18 | 83.88 | 5.34 | 26.23 | 55.68 |
| Fig. 6(b) (640 × 304) | 16.08 | 3.64 | 6.52 | 64.97 | 63.9 | 4.13 | 20.03 | 42.58 |

satisfactory result with speckle reduction, but it is obvious that the corresponding residual noise is greater than that of WGLRR, FoSVS, DnCNN, and the proposed method. WGLRR, FoSVS, DnCNN, and our method all produce despeckling results that are generally more visually appealing than SBSDI, TGV, CWDL, and PNLM do. As displayed in Fig. 9(a)–(h) and Fig.10(a)–(h), the results of WGLRR and DnCNN are over-smoothed. The layer structure is too smooth, and the inter-layer transition pointed out by the red arrow is very vague. By contrast, our method and FoSVS can effectively preserve the layer feature.

In practice, ground truth images are not easy to acquire. Therefore, the metric [63], which is the non-reference image-based method, is adopted to measure the effectiveness of each algorithm on real OCT images and is defined as shown in Eq. (37) below:

$$Q = s_1 \frac{s_1 - s_2}{s_1 + s_2} \tag{37}$$

where $s_1$ and $s_2$ are the singular values of the gradient matrix over a square window [63], respectively. A larger Q value for the despeckling approach indicates that a better speckle suppression result is obtained. The metric Q, together with the ENL and CNR of all methods, is listed in Tables 3 and 4. It is easy to find that the CNR, ENL, and metric Q of our method are larger than those of other methods in terms of the selected real OCT images. It can be inferred to a certain extent that our algorithm can obtain speckle noise suppression and feature preservation results. In Table 5, the time costs of our algorithm and others are provided. One can find that the time cost of our algorithm is shorter than that of FoSVD and WGLRR but longer than that of PNLM, DnCNN, SBSDI, TGV, and CWDL.

### 4.3. Performance evaluation

The above experimental results have visually and quantitatively illustrated the despeckling effectiveness of the presented algorithm. To more fully assess how well our algorithm performs on the preservation of image edges, the Canny edge detector, integrated in Matlab with the default parameter values, is utilized to extract the edge information from the results of all despeckling methods. The extracted edge information of Fig. 7(a)-(h) and Fig. 8(a)–(h) is shown in Fig. 11(a)-(h) and Fig. 12(a)-h), respectively. It is evident that our method performs despeckling in the background regions more effectively than other methods. As for the layer structure of the filtered images, our method and the FoSVS method have better preservation capabilities. By contrast, other comparable methods either have insufficient speckle noise suppression or an unclear layer structure (see Fig. 12).

### 4.4. Effect of parameters

As seen in the previous section, our algorithm obtains a better despeckling performance with fixed parameters, which is mainly

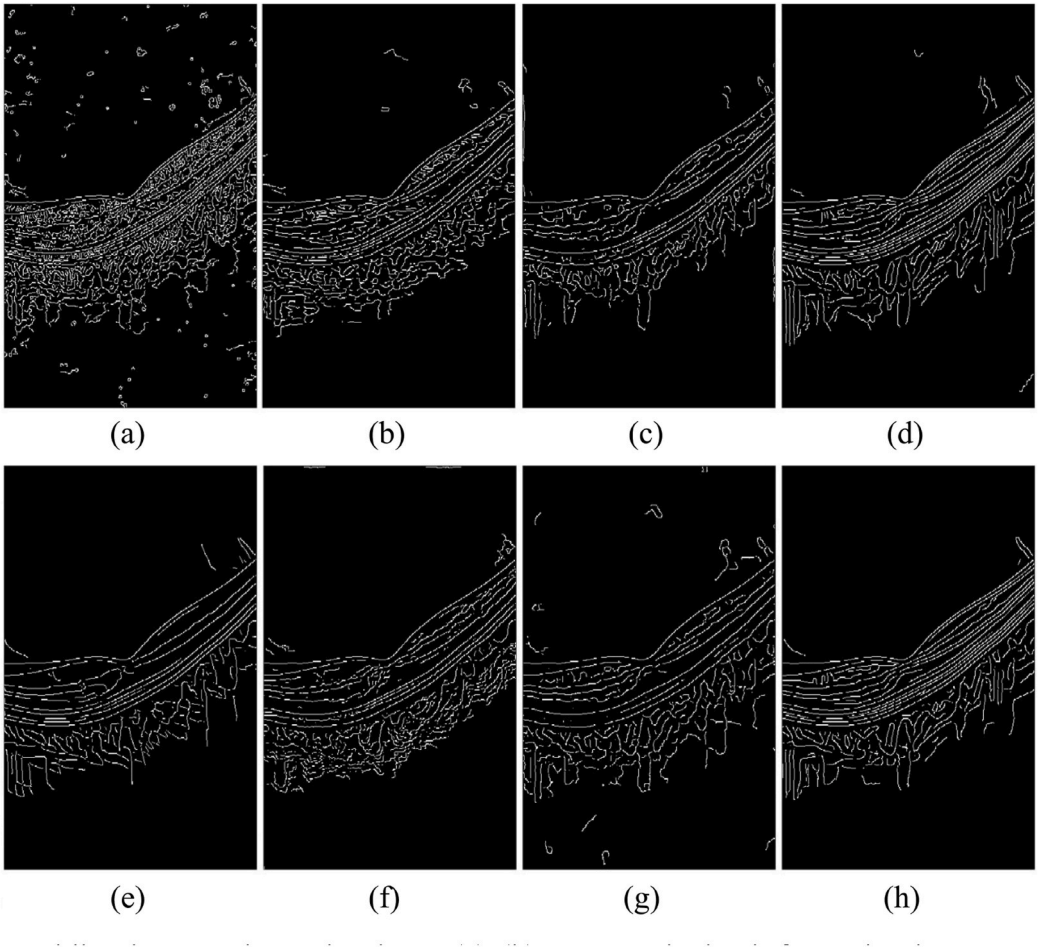


**Fig. 11.** Edge maps of despeckling images shown in Fig. 7. (a)–(h) Extracted edge information by PNLM [30], SBSDI [32], TGV, FoSVS [20], WGLRR [39], DnCNN [43], CWDL [36], and our method, respectively.

determined after conducting numerous experiments. To further illustrate the effect of parameters on our model for speckle noise suppression, we list the results of SSIM, PSNR, XCOR, and EPI of our algorithm under different settings of these parameters, as shown in Tables 6–9. It is worth noting that Tables 6–9 only report the average metrics of the dataset [32], which contains 18 test images. In addition, testing all combinations of parameters seems like an impossible task. Therefore, we keep the other parameters unchanged and change the value of one of them. From Tables 6 and it can be seen that there is no change in these metrics. In other words, the proposed method has strong robustness for the scaling factor $\lambda$. As can be seen in Table 7, SSIM reaches its maximum value when regulation parameter $\gamma$ is 7. And PSNR, XCOR, and EPI change very little when $\gamma$ is greater than 7. As seen in Table 8, increasing image patch size will increase the values of SSIM and PSNR, but those of XCOR and EPI will increase more slowly. The parameter $n_3$ determines how many similar patches are included in the constructed 3D tensor, and the effect of $n_3$ on metrics is listed in Table 9. Based on the numerical results, we can find that PSNR increases as $n_3$ increases; however, SSIM reaches its maximum value when $n_3$ is set to 60. A fact that cannot be ignored is that the computational cost increases dramatically with increasing $n$ and $n_3$. To balance the running complexity and the despeckling effectiveness of the presented method, we set the parameters as below: $n = 11$, $n_3 = 60$, $\gamma = 7$ and $\lambda = 0.6$, and these parameters remain constant in all experiments.

## 5. Conclusion

A *t*-SVD based two-stage speckle noise suppression method is presented to effectively reconstruct the noisy input OCT images. And speckle noise in both real and synthetic OCT images is initially removed in the first stage. To effectively enhance the speckle suppression results, in the second stage, we define an adaptive projection parameter and construct a feature-guided thresholding strategy that can well suppress speckle noise and retain the image structural features. Additionally, the presented algorithm outperforms several comparison methods in relation to speckle suppression and objective metrics. However, the proposed method suffers from some limitations. For example, the currently used Matlab implementation of our method has no running-time advantages. And a lot of experiments need to be performed to find the parameters that balance the various performances. As a result, further research has to be

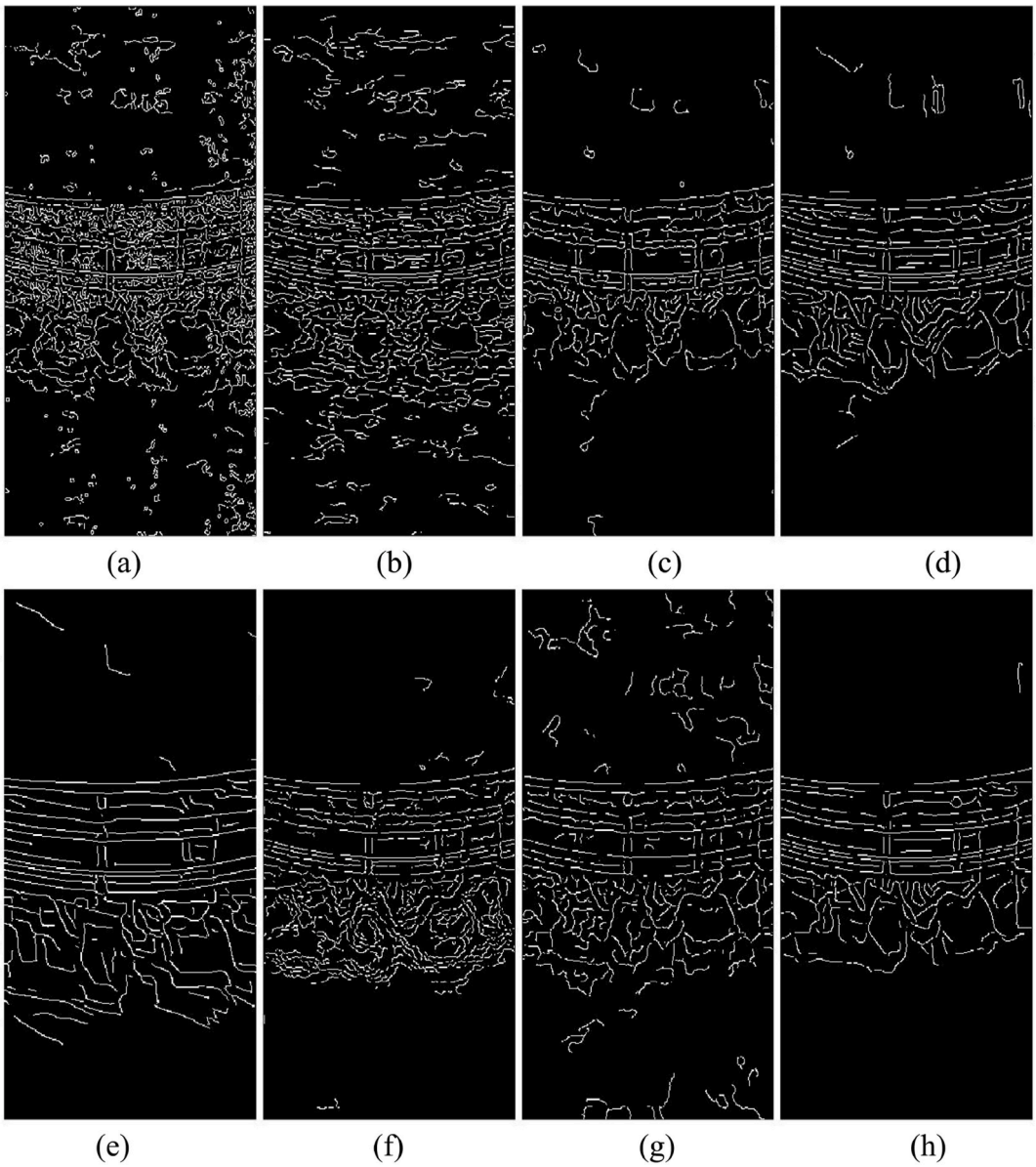


**Fig. 12.** Edge maps of despeckling images shown in Fig. 8. (a)–(h) Extracted edge information by PNLM [30], SBSDI [32], TGV, FoSVS [20], WGLRR [39], DnCNN [43], CWDL [36], and our method, respectively.

**Table 6**
Effect of the parameter $\lambda$.

| Metrics | Scaling factor $\lambda$ defined in Eq. (12) | | | | | | |
|---|---|---|---|---|---|---|---|
| | 0.3 | 0.4 | 0.5 | 0.6 | 0.7 | 0.8 | 0.9 |
| PSNR | 28.3707 | 28.3707 | 28.3707 | 28.3707 | 28.3707 | 28.3707 | 28.3707 |
| SSIM | 0.6975 | 0.6975 | 0.6975 | 0.6975 | 0.6975 | 0.6975 | 0.6975 |
| XCOR | 0.9838 | 0.9838 | 0.9838 | 0.9838 | 0.9838 | 0.9838 | 0.9838 |
| EPI | 0.3812 | 0.3812 | 0.3812 | 0.3812 | 0.3812 | 0.3812 | 0.3812 |

**Table 7**
Effect of the parameter $\gamma$.

| Metrics | Regulation parameter $\gamma$ defined in Eq. (13) | | | | | | |
|---|---|---|---|---|---|---|---|
| | 1 | 3 | 5 | 7 | 9 | 11 | 13 |
| PSNR | 28.1923 | 28.3063 | 28.3532 | 28.3707 | 28.3766 | 28.3766 | 28.3798 |
| SSIM | 0.6808 | 0.6924 | 0.6965 | 0.6975 | 0.6974 | 0.6973 | 0.6973 |
| XCOR | 0.9934 | 0.9936 | 0.9937 | 0.9938 | 0.9938 | 0.9938 | 0.9938 |
| EPI | 0.3267 | 0.3619 | 0.3765 | 0.3812 | 0.3820 | 0.3822 | 0.3822 |

**Table 8**
Effect of the parameter $n$.

| Metrics | Size of image patch $n$ | | | | | | |
|---|---|---|---|---|---|---|---|
| | 5 | 7 | 9 | 11 | 13 | 15 | 17 |
| PSNR | 27.6895 | 28.1956 | 28.3045 | 28.3707 | 28.4144 | 28.4411 | 28.4589 |
| SSIM | 0.6721 | 0.6926 | 0.6959 | 0.6975 | 0.6982 | 0.6987 | 0.6991 |
| XCOR | 0.9931 | 0.9936 | 0.9937 | 0.9938 | 0.9938 | 0.9938 | 0.9938 |
| EPI | 0.2738 | 0.3747 | 0.3798 | 0.3812 | 0.3816 | 0.3819 | 0.3821 |

**Table 9**
Effect of the parameter $n_3$.

| Metrics | Size of image patch $n_3$ | | | | | | |
|---|---|---|---|---|---|---|---|
| | 30 | 40 | 50 | 60 | 70 | 80 | 90 |
| PSNR | 28.2978 | 28.3297 | 28.3542 | 28.3707 | 28.3815 | 28.3874 | 28.3908 |
| SSIM | 0.6966 | 0.6972 | 0.6974 | 0.6975 | 0.6974 | 0.6973 | 0.6972 |
| XCOR | 0.9936 | 0.9937 | 0.9937 | 0.9938 | 0.9938 | 0.9938 | 0.9938 |
| EPI | 0.3735 | 0.3744 | 0.3798 | 0.3812 | 0.3817 | 0.3819 | 0.3820 |

done in the future about the criteria for determining the parameters.

In addition, there are also some interesting future works. Compared with the convex models, the nonconvex models in the low-rank framework generally give better results in speckle noise reduction. Hence, the extensions to nonconvex cases can be interesting. And it is also interesting to use the developed method for the processing of various other kinds of information, for example, bioinformatics, web data, and videos.

## Author contribution statement

Ying Fang, Xia Shao, Bangquan Liu, Hongli Lv: Conceived and designed the experiments; Performed the experiments; Analyzed and interpreted the data; Contributed reagents, materials, analysis tools or data; Wrote the paper.

## Funding statement

This research was funded by Key scientific research projects of Higher Education Institutions of Henan Province [21A520037; 21A520038], Henan Province Key R&D and Promotion Special [202,102,110,275; 222,102,210,183], Zhejiang Provincial Natural Science Foundation of China [LY20F020005], Zhejiang Provincial Philosophy and Social Sciences Planning Project [21NDJC021Z], Natural Science Foundation of Ningbo city [202003N4072], Research Start-up Fund Grant Project of Shangqiu Normal University [700,172].

## Data availability statement

Data included in article/supp. Material/referenced in article.

## Additional information

No additional information is available for this paper.

## Declaration of competing interest

The authors declare that they have no known competing financial interests or personal relationships that could have appeared to influence the work reported in this paper.

## Acknowledgments

The authors are grateful to M. Li, Y. Chen, K. Xie, S. Yuan, and Q. Chen for the release of OCT datasets.

## References

[1] D. Huang, E.A. Swanson, C.P. Lin, J.S. Schuman, W.G. Stinson, W. Chang, M.R. Hee, T. Flotte, K.W. Gregory, C.A. Puliafito, J.G. fujimoto, Optical coherence tomography, Science 254 (5035) (1991) 1178–1181.
[2] J. Schmitt, Optical coherence tomography (OCT): a review, IEEE J. Sel. Top. Quant. Electron. 5 (4) (1999) 1205–1215.
[3] C.A. Puliafito, M.R. Hee, C.P. Lin, E. Reichel, J.S. Schuman, J.S. Duker, J.A. Izatt, E.A. Swanson, J.G. Fujimoto, Imaging of macular diseases with optical coherence tomography, Ophthalmology 102 (2) (1995) 217–229.
[4] W. Drexler, U. Morgner, R.K. Ghanta, F.X. Kartner, J.S. Schuman, J.G. Fujimoto, Ultrahigh-resolution ophthalmic optical coherence tomography, Nat. Med. 7 (4) (2001) 502–507.
[5] H. Lv, S. Fu, C. Zhang, L. Zhai, Speckle noise reduction of multi-frame optical coherence tomography data using multi-linear principal component analysis, Opt Express 26 (9) (2018) 11804–11818.
[6] H. Lv, S. Fu, C. Zhang, L. Zhai, Speckle noise reduction for optical coherence tomography based on adaptive 2D dictionary, Laser Phys. Lett. 15 (5) (2018), 055401.
[7] H. Chen, S. Fu, H. Wang, Y. Li, F. Wang, Speckle reduction based on fractional-order filtering and boosted singular value shrinkage for optical coherence tomography image, Biomed. Signal Process Control 52 (2019) 281–292.
[8] H. Chen, Fusion denoising algorithm of optical coherence tomography image based on point-estimated and block-estimated, Optik 225 (2021), 165864.
[9] M. Pircher, E. Gotzinger, R.A. Leitgeb, A.F. Fercher, C.K. Hitzenberger, Speckle reduction in optical coherence tomography by frequency compounding, J. Biomed. Opt. 8 (3) (2003) 565–569.
[10] D. Cui, E. Bo, Y. Luo, X. Liu, X. Wang, S. Chen, L. Liu, Multifiber angular compounding optical coherence tomography for speckle reduction, Opt. Lett. 42 (1) (2017) 125–128.
[11] C. Chen, W. Shi, R. Deorajh, N. Nguyen, J. Ramjist, A.J. Marques, V.X.D. Yang, Beam-shifting technique for speckle reduction and flow rate measurement in optical coherence tomography, Opt. Lett. 43 (24) (2018) 5921–5924.
[12] B.F. Kennedy, T.R. Hillman, A. Curatolo, D.D. Sampson, Speckle reduction in optical coherence tomography by strain compounding, Opt. Lett. 35 (14) (2010) 2445–2447.
[13] W. Shi, C. Chen, J. Jivraj, Y. Dobashi, W. Gao, V.X.D. Yang, 2D MEMS-based high-speed beam-shifting technique for speckle noise reduction and flow rate measurement in optical coherence tomography, Opt Express 27 (9) (2019) 12551–12564.
[14] Y. Zhao, K.K. Chu, W.J. Eldridge, E.T. Jelly, M. Crose, A. Wax, Real-time speckle reduction in optical coherence tomography using the dual window method, Biomed. Opt Express 9 (2) (2018) 616–622.
[15] R. Li, H. Yin, J. Hong, C. Wang, B. He, Z. Chen, Q. Li, P. Xue, X. Zhang, Speckle reducing OCT using optical chopper, Opt Express 28 (3) (2020) 4021–4031.
[16] N. Anantrasirichai, L. Nicholson, J.E. Morgan, I. Erchova, K. Mortlock, R.V. North, A. Achim, Adaptive-weighted bilateral filtering and other preprocessing techniques for optical coherence tomography, Comput. Med. Imag. Graph. 38 (6) (2014) 526–539.
[17] A. Ozcan, A. Bilenca, A.E. Desjardins, B.E. Bouma, G.J. Tearney, Speckle reduction in optical coherence tomography images using digital filtering, J. Opt. Soc. Am. 24 (7) (2007) 1901–1910.
[18] G. Gong, H. Zhang, M. Yao, Speckle noise reduction algorithm with total variation regularization in optical coherence tomography, Opt Express 23 (9) (2015) 24699–24712.
[19] T. Wu, Y. Shi, Y. Liu, C. He, Speckle reduction in optical coherence tomography by adaptive total variation method, J. Mod. Opt. 62 (2) (2015) 1849–1855.
[20] J. Duan, W. Lu, C. Tench, I. Gottlob, F. Proudlock, N.N. Samani, L. Bai, Denoising optical coherence tomography using second order total generalized variation decomposition, Biomed. Signal Process Control 24 (2016) 120–127.
[21] R. Bernardes, C. Maduro, P. Serranho, A. Araujo, S. Barbeiro, J. Cunha-Vaz, Improved adaptive complex diffusion despeckling filter, Opt Express 18 (23) (2010) 24084, 24059.
[22] M. Xu, C. Tang, M. Chen, Y. Qiu, Z. Lei, Texture preservation and speckle reduction in optical coherence tomography using the shearlet-based total variation algorithm, Opt Laser. Eng. 122 (2019) 265–283.
[23] J. Yang, Y. Hu, L. Fang, J. Cheng, J. Liu, Universal digital filtering for denoising volumetric retinal OCT and OCT angiography in 3D shearlet domain, Opt. Lett. 45 (3) (2019) 694–697.
[24] F. Zaki, Y. Wang, H. Su, X. Yuan, X. Liu, Noise adaptive wavelet thresholding for speckle noise removal in optical coherence tomography, Biomed. Opt Express 8 (5) (2017) 2720–2731.
[25] Z. Jian, Z. Yu, L. Yu, B. Rao, Z. Chen, B.J. Tromberg, Speckle attenuation in optical coherence tomography by curvelet shrinkage, Opt. Lett. 34 (4) (2009) 1516–1518.
[26] A.C. Chan, K. Kurokawa, S. Makita, M. Miura, Y. Yasuno, Maximum a posteriori estimator for high-contrast image composition of optical coherence tomography, Opt. Lett. 41 (2) (2016) 321–324.
[27] A.C. Chan, Y.J. Hong, S. Makita, M. Miura, Y. Yasuno, Noise-bias and polarization-artifact corrected optical coherence tomography by maximum a-posteriori intensity estimation, Biomed. Opt Express 8 (4) (2017) 2069–2087.
[28] M. Samieinasab, Z. Amini, H. Rabbani, Multivariate statistical modeling of retinal optical coherence tomography, IEEE Trans. Med. Imag. 39 (11) (2020) 3475–3487.
[29] Q. Chen, L. de Sisternes, T. Leng, D.L. Rubin, Application of improved homogeneity similarity-based denoising in optical coherence tomography retinal images, J. Digit. Imag. 28 (3) (2015) 346–361.
[30] H. Yu, J. Gao, A. Li, Probability-based non-local means filter for speckle noise suppression in optical coherence tomography images, Opt. Lett. 41 (5) (2016) 994–997.
[31] Y. Gu, X. Zhang, Spiking cortical model based non-local means method for despeckling multiframe optical coherence tomography data, Laser Phys. Lett. 14 (5) (2017), 056201.
[32] L. Fang, S. Li, R.P. McNabb, Q. Nie, A.N. Kuo, C.A. Toth, J.A. Izatt, S. Farsiu, Fast Acquisition and reconstruction of optical coherence tomography images via sparse representation, IEEE Trans. Med. Imag. 32 (11) (2013) 2034–2049.
[33] L. Fang, S. Li, Q. Nie, J.A. Izatt, C.A. Toth, S. Farsiu, Sparsity based denoising of spectral domain optical coherence tomography images, Biomed. Opt Express 3 (5) (2012) 927–942.
[34] A. Abbasi, A. Monadjemi, L. Fang, H. Rabbani, Optical coherence tomography retinal image reconstruction via nonlocal weighted sparse representation, J. Biomed. Opt. 23 (3) (2018), 036011.
[35] X. Zhang, Z. Li, N. Nan, X. Wang, Denoising algorithm of OCT images via sparse representation based on noise estimation and global dictionary, Opt Express 30 (4) (2022) 5788–5802.
[36] R. Kafieh, H. Rabbani, I. Selesnick, Three dimensional data-driven multi scale atomic representation of optical coherence tomography, IEEE Trans. Med. Imag. 34 (5) (2014) 1042–1062.
[37] H. Chen, S. Fu, H. Wang, H. Lv, C. Zhang, F. Wang, Y. Li, Feature-oriented singular value shrinkage for optical coherence tomography image, Opt Laser. Eng. 114 (2019) 111–120.
[38] H. Chen, S. Fu, H. Wang, H. Lv, C. Zhang, Speckle attenuation by adaptive singular value shrinking with generalized likelihood matching in optical coherence tomography, J. Biomed. Opt. 23 (3) (2018), 036014.

[39] C. Tang, L. Cao, J. Chen, X. Zheng, Speckle noise reduction for optical coherence tomography images via non-local weighted group low-rank representation, Laser Phys. Lett. 14 (5) (2017), 056002.
[40] Y. Ma, X. Chen, W. Zhu, X. Cheng, D. Xiang, F. Shi, Speckle noise reduction in optical coherence tomography images based on edge-sensitive cGAN, Biomed. Opt Express 9 (11) (2018) 5129–5146.
[41] F. Shi, N. Cai, Y. Gu, D. Hu, Y. Ma, Y. Chen, X. Chen, DeSpecNet: a CNN-based method for speckle reduction in retinal optical coherence tomography images, Phys. Med. Biol. 64 (17) (2019), 175010.
[42] B. Qiu, Z. Huang, X. Liu, X. Meng, Y. You, G. Liu, K. Yang, A. Maier, Q. Ren, Y. Lu, Noise reduction in optical coherence tomography images using a deep neural network with perceptually-sensitive loss function, Biomed. Opt Express 11 (2) (2020) 817–830.
[43] K. Zhang, W. Zuo, Y. Chen, D. Meng, L. Zhang, Beyond a Gaussian denoiser: residual learning of deep CNN for image denoising, IEEE Trans. Image Process. 26 (7) (2017) 3142–3155.
[44] M.E. Kilmer, C.D. Martin, Factorization strategies for third-order tensors, Linear Algebra Appl 45 (3) (2011) 641–658.
[45] C. Lu, J. Feng, Y. Chen, W. Liu, Z. Lin, S. Yan, Tensor robust principal component analysis with a new tensor nuclear norm, IEEE Trans. Pattern Anal. Mach. Intell. 42 (4) (2020) 925–938.
[46] M.E. Kilmer, K. Braman, N. Hao, R.C. Hoover, Third-order tensors as operators on matrices: a theoretical and computational framework with applications in imaging, SIAM J. Matrix Anal. Appl. 34 (1) (2013) 148–172.
[47] Z. Kong, L. Han, X. Liu, X. Yang, A new 4-D nonlocal transform-domain filter for 3-D magnetic resonance images denoising, IEEE Trans. Med. Imag. 37 (4) (2008) 941–954.
[48] Z. Zhang, S. Aeron, Exact tensor completion using t-SVD, IEEE Trans. Signal Process. 65 (6) (2016) 1511–1526.
[49] C. Zhang, W. Hu, T. Jin, Z. Mei, Nonlocal image denoising via adaptive tensor nuclear norm minimization, Neural Comput. Appl. 29 (1) (2018) 3–19.
[50] K. Gilman, D.A. Tarzanagh, L. Balzano, Grassmannian optimization for online tensor completion and tracking with the t-SVD, IEEE Trans. Signal Process. 70 (2022) 2152–2167.
[51] N. Hao, M.E. Kilmer, K. Braman, R.C. Hoover, Facial recognition using tensor-tensor decompositions, SIAM J. Imag. Sci. 6 (1) (2013) 437–463.
[52] S. Osher, M. Burger, D. Goldfarb, J. Xu, W. Yin, An iterative regularization method for total variation based image restoration, SIAM Multiscale Model. Simul. 4 (2) (2005) 460–489.
[53] J.F. Cai, E.J. Candes, Z. Shen, A singular value thresholding algorithm for matrix completion, SIAM J. Optim. 20 (4) (2010) 1956–1982.
[54] A. Buades, B. Coll, J.M. Morel, A review of image denoising algorithms with a new one, SIAM Multiscale Model. Simul. 4 (2) (2005) 490–530.
[55] C.A. Deledalle, L. Denis, F. Tupin, How to compare noisy patches? Patch similarity beyond Gaussian noise, Int. J. Comput. Vis. 99 (1) (2012) 86–102.
[56] H. Lv, Y. Zhang, R. Wang, Active contour model based on local absolute difference energy and fractional-order penalty term, Appl. Math. Model. 107 (2022) 207–232.
[57] K.B. Oldham, J. Spanier, The Fractional Calculus, first ed., Academic Press, 1974.
[58] Q. Chen, P. Montesinos, Q. Sun, P. Heng, D. Xia, Adaptive total variation denoising based on difference curvature, Image Vis Comput. 28 (3) (2010) 298–306.
[59] L. Bian, J. Suo, F. Chen, Q. Dai, Multi-frame denoising of high-speed optical coherence tomography data using inter-frame and intra-frame priors, J. Biomed. Opt. 20 (3) (2015), 036006.
[60] A. Pizurica, L. Jovanov, B. Huysmans, V. Zlokolica, P. De Keyser, F. Dhaenens, W. Philips, Multiresolution denoising for optical coherence tomography: a review and evaluation, Curr. Med. Imag. Rev. 4 (4) (2008) 270–284.
[61] H. Lv, Speckle attenuation for optical coherence tomography images using the generalized low rank approximations of matrices, Opt Express 31 (7) (2023) 11745–11759.
[62] M. Li, Y. Chen, K. Xie, S. Yuan, Q. Chen, OCTA-500, IEEE Dataport, 2019, https://doi.org/10.1109/TMI.2020.2992244.
[63] X. Zhu, P. Milanfar, Automatic parameter selection for denoising algorithms using a no-reference measure of image content, IEEE Trans. Image Process. 19 (12) (2010) 3116–3132.